

[Click here to view linked References](#)

Magma evolution at La Fossa volcano (Vulcano Island, Italy) in the last 1000 years: evidence from eruptive products and temperature gradient experiments

Costa S.^{1,2,*}, Masotta M.², Gioncada A.², Pistolesi M.², Bosch D.³, Scarlato P.⁴

¹ Dipartimento di Scienze della Terra, Università di Firenze, via La Pira, 4 50121 Firenze, Italy

² Dipartimento di Scienze della Terra, Università di Pisa, via S. Maria, 53 56126 Pisa, Italy

³ Géosciences Montpellier, Université de Montpellier, Place E. Bataillon, 34095 Montpellier, France

⁴ Istituto Nazionale di Geofisica e Vulcanologia, Via di Vigna Murata 605, 00191 Roma, Italy

*corresponding author simone.costa@unifi.it, ORCID 000-0003-2268-2906

Abstract

The intense explosive and effusive volcanic activity of the last 1000 years at La Fossa volcano (Vulcano Island, Italy) was characterized by the eruption of magmas ranging in composition from latites to trachytes and rhyolites, as well as K-rich trachytes. Evidence of sin-eruptive mixing among these magmas are frequently observed in the form of magmatic enclaves and bands in lava flows and pyroclastic products. The petrological and volcanological diversity of the erupted materials suggests that complex differentiation processes occurred in the shallow part of the plumbing system. With the aim to reconstruct the magmatic feeding system and to identify the differentiation processes behind such a petrologic complexity, we analyzed lavas and pyroclastic products representative of the recent eruptive sequences at La Fossa and combined the petro-chemical features with thermo-barometric calculations, geochemical modelling and temperature gradient experiments. Thermo-barometric calculations indicate that the K-rich trachytic magma crystallized at lower pressure (160 ± 54 MPa) compared to the latitic (307 ± 47 MPa) and trachytic (208 ± 30 MPa) magmas. Differentiation modelling suggests that both trachytic and rhyolitic compositions can be obtained through differentiation of a common latitic magma, essentially by varying the plagioclase/sanidine ratio. Temperature gradient experiments, performed at the conditions inferred for the shallow plumbing system of La Fossa volcano (150 MPa and 1050-900 °C), indicate different paths of melt differentiation that overall produce an increase of the $\text{SiO}_2/\text{K}_2\text{O}$ ratio with the increasing H_2O in the system (from 0 to 4 wt.%). This is consistent with the origin of K-rich trachytes at lower pressure and lower H_2O content. In turn, the formation of crystal-poor rhyolites is explained by segregation of the interstitial melt formed in a latitic-trachytic crystal mush, favored by the second boiling of the melt and consequent exsolution of a fluid phase.

Keywords: Vulcano island, trachyte, crystal-poor rhyolite, crystal mush, temperature gradient experiments

1. Introduction

The physico-chemical characterization of the plumbing system of frequently active arc volcanoes is one of the main challenges in volcanology, as it constitutes a ground element for the assessment of the pre-eruptive conditions of magmas and for the definition of future eruptive scenarios. On the one hand, the estimate of the intensive variables of the magma is possible either through the thermo-barometric calculations based on the phase compositions of eruptive products (Putirka 2008), or via direct comparison of the natural products with laboratory experiments performed under constrained physical conditions (Scaillet et al. 2008). On the other hand, clues on the chemical composition of magmas feeding the eruptions can be obtained through the petrologic study of the eruptive products of the recent volcanic activity (Cioni et al. 1998). Such information, combined with data obtained from the geochemical and geophysical monitoring, are critical for determining the variations of the physico-chemical parameters of magmas and, ultimately, for the volcanic hazard assessment and for designing risk mitigation plans (Neri et al. 2008). In this context, the active volcanic system of La

45 Fossa (Vulcano island, Italy), with its recurrent historic activity and well-known stratigraphy (De Astis et al. 2013),
46 represents an ideal study case for the investigation of magmatic processes and eruptive dynamics.

47 The eruptive products of La Fossa encompass a broad range of magma compositions, ranging from latite to trachyte
48 and rhyolite. The heterogeneous composition of magmas erupted even within single eruptions, testifies to sin-eruptive
49 mixing and or mingling processes (De Astis et al. 2013). Latitic to trachytic magmatic enclaves in rhyolitic lavas and
50 compositionally heterogeneous (banded) pumices are in fact common in the recent activity of La Fossa volcano (e.g.
51 Piochi et al. 2009; Rossi et al. 2019). Significant variations of magma chemistry at a same SiO₂ content are also observed,
52 as in the case of the fallout products emplaced during the Palizzi-Commenda eruptive cluster (Di Traglia et al. 2013),
53 whose trachytic composition has the highest concentration in K₂O of the entire eruptive history of La Fossa volcano (up
54 to 7.5 wt.%; Fulignati et al. 2018).

55 The petrological complexity of the plumbing system of La Fossa has been the object of many studies in the past two
56 decades, aimed at defining: i) the intensive variables and the magmatic processes governing the evolution of parental
57 magmas (Clocchiatti et al. 1994; De Astis et al. 1997; Del Moro et al. 1998; Gioncada et al. 1998; Pinarelli et al. 2019);
58 ii) the pre- and syn-eruptive interaction of magmas at different degrees of evolution (Piochi et al. 2009; Bullock et al.
59 2019); and iii) the dynamics and time scales of pre-eruptive magma ascent, mixing and eruption (Vetere et al. 2015;
60 Nicotra et al. 2018; Rossi et al. 2019). Although there is a general consensus for the pre-eruptive temperature estimates
61 and mixing processes of the latitic, trachytic and rhyolitic magmas erupted at La Fossa (Clocchiatti et al. 1994; Vetere et
62 al. 2015), uncertainty in the determination of pressure of magma storage and volatile content and in the overall
63 relationships among these magmas still exists. This gap of knowledge is in part explained by the fact that most of
64 petrologic studies are focused on lava flows and on the youngest explosive products, which are more easily accessible
65 and better constrained from a chrono-stratigraphic point of view. This inevitably leads to underestimating the significance
66 of the pyroclastic component (e.g. fallout deposits) that constitute the largest fraction of the volume of erupted magmas
67 (Di Traglia et al. 2013). Through the analysis of the pyroclastic products and their distribution in the eruptive sequence it
68 is thus possible to obtain a broader picture of the plumbing system to place constraints on magma dynamics and evolution
69 in small arc volcanoes.

70 In this study, we took in exam the last 1000 years activity of La Fossa volcano, with the aim of reconstructing the
71 physical conditions at which magmas evolved, interacted and erupted. For this purpose, we selected representative rock
72 samples encompassing the entire compositional range of erupted magmas, and combined new whole rock and micro-
73 chemical analyses of natural samples with temperature gradient experiments, that emulate the crystallization and
74 differentiation processes occurring in a shallow and temperature-zoned magma reservoir. The results obtained in this
75 work contribute to envisage the complexity of the polybaric storage system of La Fossa volcano, where the role of shallow
76 crystal mushes is determinant for the production of small volumes of rhyolitic magmas at rather short time scale, through
77 repeated episodes of melt extraction.

51 2. Geological background and stratigraphy of the last 1000 years of La Fossa

52 Vulcano is the southernmost island of the Aeolian archipelago, a volcanic arc located in southern Tyrrhenian sea (Fig.
53 1). La Fossa cone, located in the northern sector of the island and active since 6 ka, last erupted in AD 1888-1890 (Keller
54 1980). The stratigraphy of La Fossa cone has been described in detail in many studies and consists mainly of pyroclastic
55 fallout deposits (ash, pumiceous lapilli, blocks and breadcrust bombs) and lava flows (Clocchiatti et al. 1994; Piochi et
56 al. 2009; Di Traglia et al. 2013; De Astis et al. 2013). Following the stratigraphic reconstruction proposed by Di Traglia
57 et al. (2013), the eruptive history of the last 1000 years can be summarized in two eruptive clusters: the Palizzi-Commenda
58
59
60
61

86 eruptive cluster (PCEC), developed during the 13th century, and the Gran Cratere eruptive cluster (GCEC, 15th century-
187 1890 AD) (Fig. 2a). The stratigraphic sequence of PCEC displays a large variety of eruptive products and a wide spectrum
2 38 of magma compositions, ranging from latite to trachyte and rhyolite (Fig. 2b): i) latitic and trachytic cross-stratified and
49 parallel-bedded ash layers (Pal A and Pal C); ii) pumiceous fallout layers of rhyolitic and trachytic composition (Pal B
5 and Pal D, respectively); iii) lava flows, including the rhyolitic obsidian Commenda lava and the trachytic lava flows of
91 Palizzi, Campo Sportivo and Punte Nere; iv) ash layers and widely dispersed pyroclastic density currents deposits
8 associated to the hydrothermal eruption of Breccia di Commenda (Gurioli et al. 2012; Rosi et al. 2018). The GCEC
92 includes the products of the Pietre Cotte eruptive unit, consisting of: i) latitic ash and lapilli layers; ii) rhyolitic pumiceous
103 fallout layers iii) the rhyolitic AD 1739 Pietre Cotte lava flow (Piochi et al. 2009; Vetere et al. 2015). The uppermost part
11 124 of the GCEC is represented by the products of the AD 1888-1890 eruption, consisting of latitic spatters, trachytic and
13 145 rhyolitic ash and lapilli layers and the characteristic breadcrust bombs, trachytic and rhyolitic in composition (Clocchiatti
14 et al. 1994).

19 20 21 22 23 24 25 26 27 28 29 30 31 32 33 34 35 36 37 38 39 40 41 42 43 44 45 46 47 48 49 50 51 52 53 54 55 56 57 58 59 60 61 62 63 64 65

2.2 La Fossa plumbing system

The plumbing system of La Fossa cone has been object of several studies that reported petrological evidences of
magma mixing processes, such as the occurrence of magmatic enclaves and banding of latitic and trachytic compositions
within rhyolitic lava flows and pyroclastic products (Frazzetta et al. 1983; De Fino et al. 1991; Clocchiatti et al. 1994;
Piochi et al. 2009; De Astis et al. 2013; Bullock et al. 2019; Rossi et al. 2019). The combination of petrological and
geochemical data, including melt, fluid inclusions and gas geochemistry (Clocchiatti et al. 1994; Gioncada et al. 1998;
Zanon et al. 2003; Paonita et al. 2013; Mandarano et al. 2016), contributed to envisage the plumbing system of La Fossa
as a complex polybaric system, represented by multiple reservoirs that have been variably involved during the activity of
both La Fossa and Vulcanello (Peccerillo et al. 2006; Davì et al. 2009; De Astis et al. 2013; Fusillo et al. 2015; Nicotra
et al. 2018). The deepest reservoir (basaltic to shoshonitic) is presumably located between 21 and 18 km, whereas a
shoshonitic to latitic storage level has been hypothesized between ~17 and 12 km (De Astis et al. 2013; Nicotra et al.
2018). The shallow crustal reservoirs hosting latitic to trachytic and rhyolitic magmas are presumably located at depths
comprised between 5 and 2 km. Based on a recent calibration of a plagioclase-liquid hygrometer, Masotta and Mollo
(2019) estimated H₂O contents ranging from 2.5 to 3.5 wt.% for the latitic and trachytic magmas, respectively. An
uppermost rhyolitic reservoir located at depth of about 1-2 km has been suggested by Clocchiatti et al. (1994) and Zanon
et al. (2003) based on the study of secondary fluid inclusions found in metamorphic xenoliths, yielding to equilibration
pressure and temperature of 30-60 MPa and ~1000 °C, respectively. Based on thermodynamic modelling, Vetere et al.
(2015) estimated the pre-eruptive temperature of latitic and rhyolitic magmas involved in the mixing process leading to
the extrusion of the AD 1739 Pietre Cotte lava flow, obtaining temperature of about 1010 °C for the latite and 950 °C for
the rhyolite. In contrast, thermometric analyses on melt inclusions by Clocchiatti et al. (1994) indicate crystallization
temperatures of 1100±10 and 1050±10 °C respectively for the latite and trachyte involved in the AD 1888-1890 eruption.
These values are in agreement with the temperature range 1000-1130 °C inferred by Bullock et al. (2019) for lati-trachytic
magmas of Pietre Cotte, but is in excess compared to other recent temperature estimates for trachytic magmas of the
recent activity (Palizzi, Pietre Cotte and AD 1888-1890) that indicate temperatures between 950 and 1000 °C (Fulignati
et al. 2018; Masotta and Mollo 2019).

3. Materials and methods

3.1 Sampling

Samples were selected among the last 1000 years eruptive products of La Fossa, in order to cover the whole compositional spectrum of the erupted magmas. Samples from PCEC include the rhyolitic and trachytic pumices from the fallout layers (Pal B and Pal D, respectively) and the trachytic Palizzi lava flow. Samples from GCEC include the latitic enclaves contained in the obsidian of Pietre Cotte. The lava samples were prepared in thin sections for petrographic and microchemical analyses. The pumiceous lapilli were crushed and crystals with their host glass were manually separated under a stereomicroscope, embedded in epoxy mounts and polished for microanalysis. Sample powders were prepared by selecting aliquots of samples that did not show mixing features (e.g. compositional banding and enclaves), crushed and pulverized using a planetary mill at the Dipartimento di Scienze della Terra at the Università di Pisa and used for X-Ray fluorescence (XRF) and ICP-MS analyses.

3.2 Temperature gradient experiments

Temperature gradient experiments were performed at the HP-HT Laboratory of Experimental Volcanology and Geophysics of Istituto Nazionale di Geofisica e Vulcanologia (Rome, Italy) in a non-end loaded piston cylinder (QUICKpress type), using a 19-25 mm assembly designed for experiments at pressure between 150 and 300 MPa (Masotta et al. 2012a). Temperature gradient experiments take advantage of the intrinsic temperature gradient of piston cylinder furnaces. The temperature profile of the experimental assembly was previously measured by Masotta et al. (2012b). This experimental strategy has been adopted by several authors to investigate the effect of temperature gradient on melt differentiation, isotopic fractionation and fluid transport in magmas (Huang et al. 2009; Masotta et al. 2012b; Rodriguez et al. 2015, 2017; Laumonier et al. 2019). Experiments were performed at the pressure of 150 MPa, with temperature ranging from 1050 °C at the bottom of the capsule (hot spot) to 900 °C at the top, with constant run duration of 24 h. The temperature of the hot spot was constantly monitored using a C-type thermocouple, with a precision of 5 °C. At the beginning of the experiments, the temperature was increased to 1300 °C at a rate of 80 °C/min and held 30 minutes at this temperature, in order to anneal the crystal nuclei formed during the heating and to allow melt homogenization (Masotta et al. 2020). The temperature was then decreased to the experimental resting temperature with the same rate of 80 °C/min. Experiments were performed using 5 mm OD Pt capsules, at both anhydrous and hydrous (H₂O= 2 and 4 wt.%) conditions. Deionized H₂O was added in the hydrous charge using a micro-syringe, yielding to a precision of about 0.1 wt.%. The weight of the capsule was checked before and after welding, and after 30 min at 110 °C to ensure that water did not escape during capsule preparation. As starting materials, we used a glass obtained by melting at 1400 °C for 1 hour a latitic enclave from the AD 1739 Pietre Cotte lava flow (Table 1; Fig. 2b). This latitic composition represents one of the less evolved magma compositions erupted at La Fossa during the last 1000 years and taken as representative of the latitic magma of La Fossa plumbing system.

3.3 Analytical methods

The polished thin sections and resin mounts of natural products and the experimental samples were studied with a petrographic microscope, carbon-coated and analysed with a Quanta 450 Field Emission-Scanning Electron Microscope (FE-SEM) installed at the Centro Interdipartimentale di Scienza e Ingegneria dei Materiali (CISIM) at Università di Pisa. Backscattered electron (BSE) images were obtained using a 20 kV filament voltage, 10 mm working distance. The freeware software package ImageJ (Image Processing and Analysis in Java, <http://rsb.info.nih.gov/ij/>) was used for image analysis of experimental products to determine the glass/crystalline phases ratio and mineral phases abundance at different temperatures on BSE images of experimental products.

168 The whole rock major element chemical composition of natural samples was determined by X-ray Fluorescence
169 (XRF) on pressed powder pellets using an ARL 9400 XP+ sequential X-ray spectrometer at Dipartimento di Scienze della
170 Terra at the Università di Pisa. The loss on ignition (LOI) was determined at 950°C. Trace elements composition of whole
171 rock has been obtained through Inductively Coupled Plasma-Mass Spectrometry (ICP-MS) analyses at the Dipartimento
172 di Scienze della Terra at the Università di Pisa.

173 The chemical composition of the starting material glass, the experimental products and mineral phases of natural
174 products was obtained using an electron probe microanalyzer (EPMA) JEOL JXA-8200, operating in wavelength
175 dispersive mode at the Dipartimento di Scienze della Terra at the Università di Milano (operative conditions were 15 kV
176 accelerating voltage, 10 nA beam current). Glasses in both natural and experimental products were analyzed with a
177 defocused electron beam of 5 µm and counting time of 5 s on background and 15 s on peak. For minerals, a beam size of
178 2 µm and counting time of 20 s on peaks and 10 s in background were used. The following standards have been adopted:
179 jadeite (Si and Na), labradorite (Al and Ca), forsterite (Mg), andradite (Fe), rutile (Ti), orthoclase (K), barite (Ba), apatite
180 (P) and spessartine (Mn). Na and K were analyzed as first elements to minimize alkali loss. Energy Dispersive System
181 (EDS) analyses were also performed with the Quanta 450 FE-SEM (20 kV filament voltage, 10 mm working distance) at
182 CISIM at Università di Pisa.

183 *In situ* trace elements analyses of the cores and rims of mineral phases of natural products were performed by mean
184 of Laser Ablation Inductively Coupled Plasma-Mass Spectrometry (LA-ICP-MS) at Géosciences Montpellier (University
185 of Montpellier), with a pulsed 193 nm ArF excimer laser (Compex 102 from LambdaPhysik) coupled to a Thermofinnigan
186 Element XR mass spectrometer. The laser was operated at a repetition rate of 8Hz using spot sizes of 85 and 110 µm and
187 a 6 J/cm² energy density. Total analysis time was 120 s with the first 80 s used for background measurement and last 40
188 s for sample ablation. Synthetic glass NIST 612 was used for external calibration. Accuracy of the analyses was monitored
189 using the standard glass BIR-1 and SiO₂ for each sample used as internal standard. Data reduction was done with the
190 software package Glitter (<http://www.glitter-gemoc.com>).

37 38 39 40 41 42 43 44 45 46 47 48 49 50 51 52 53 54 55 56 57 58 59 60 61 62 63 64 65

4. Results

4.1 Petrographic features and whole rock geochemistry

40 The recent activity of the PCEC and GCEC is characterized by the eruption of magmas that encompass a broad range
41 of composition from latite to trachyte and rhyolite when considering the TAS diagram classification (Fig. 2b). For
42 simplicity, we use petrographic and chemical features of selected samples that have been analyzed in this study as
43 representative of the occurrence of these three types of magmas in the stratigraphy of La Fossa. We focus on the enclaves
44 of Pietre Cotte obsidian as representative of the latite (since most of the latitic products have been emplaced as fine-
45 grained material, i.e. ashes), the Palizzi lava flow and Pal D fallout for the trachyte and the Pal B pumice for the rhyolite.

Latitic magma

51 The latitic magma occurs either as the juvenile component of several spatter and ash layers of PCEC and GCEC, and
52 as magmatic enclaves in the rhyolitic pumices of Palizzi (Pal B), Pietre Cotte and in the rhyolitic obsidian lava flows of
53 Commedia and Pietre Cotte (Perugini et al. 2007; Piochi et al. 2009; De Astis et al. 2013; Figs. 3a-b). The Commedia
54 lava and the pyroclastic products of Pietre Cotte contain latitic magma both as vitrophyric bands stretched and mingled
55 with the rhyolitic glass, and as rounded to blocky porphyritic enclaves with a microcrystalline groundmass. The latitic
56 magma constituting the juvenile fraction of the pyroclastic deposits and that occurring as mingled bands is variably

209 porphyritic (porphyritic index, P.I., ranging from 3 to 30%), whilst that constituting the enclaves in both lavas and pumices
210 is crystal-rich (P.I. = 25-30%). The latitic enclaves sampled within the Pietre Cotte obsidian exhibit a mineral assemblage
211 consisting of abundant euhedral to subeuhedral plagioclase (29%) and clinopyroxene (15%), olivine (3%) and rare
212 sanidine (< 1%). Apatite and Ti-magnetite are common accessories. The groundmass is constituted by microlites of
213 plagioclase and sanidine, and intergranular clinopyroxene and opaque minerals. Plagioclase and clinopyroxene
214 phenocrysts often occur in glomerophytic texture (Fig. 3b). The bulk composition has SiO₂ ranging from 57 to 59 wt.%
215 and Na₂O+K₂O ranging from 8.5 to 10 wt.% (Table 1; Fig. 2b).

216 217 *Trachytic magma*

218 The trachytic magma is represented by several lava flows (Punte Nere, Palizzi, Campo Sportivo) and pyroclastic
219 products of the PCEC (Di Traglia et al. 2013), as well as by some coarse ash layers and some pumice and bombs of the
220 AD 1888-1890 eruption of GCEC (Clocchiatti et al. 1994). The trachytic magma also occurs as mingled bands within the
221 rhyolitic pumices of the GCEC (Rossi et al. 2019). The Palizzi lava flow exhibits a porphyritic texture (P.I. ~ 20%) and
222 a mineral assemblage made up of, in order of abundance, euhedral to subhedral plagioclase (12%), sanidine (10%),
223 clinopyroxene (6%) and scarce (~1%) olivine (Fig. 3c). Glomerocrysts of plagioclase and clinopyroxene are also present.
224 The groundmass is holocrystalline and made up by sanidine and minor amounts of plagioclase and clinopyroxene. The
225 whole rock composition of Palizzi lava is trachytic with SiO₂ from 60 to 61 wt.% and Na₂O+K₂O from 9.5 to 10.4 wt.%
226 (Table 1; Fig. 2b). The pumices of Pal D fallout layer belonging to PCEC are highly vesiculated (~80 vol.%) and low
227 porphyritic (P.I. is less than 5 %). Scarce phenocrysts of plagioclase, clinopyroxene, sanidine, biotite and olivine occur
228 in a glassy groundmass (Fig. 3d), whilst Ti-magnetite, apatite and pyrrhotite are common accessories (Fulignati et al.
229 2018). A K-rich trachytic composition is exclusive of the Pal D fallout layer. The SiO₂ content of these pumices ranges
230 from 56 to 61 wt.%, with a K₂O content as high as 7.5 wt% and to a total alkali content up to 12 wt.% (Table 1; Fig. 2b).

231 232 *Rhyolitic magma*

233 The rhyolitic magma constitutes the juvenile fraction of both pyroclastic products (Pal B pumices, Pietre Cotte fallout
234 and AD 1888-90 eruption breadcrust bombs) and lava flows (Commenda and Pietre Cotte) of both PCEC and GCEC. All
235 rhyolitic products exhibit evidence of mingling with either latitic or trachytic magmas, with the rhyolitic magma
236 constituting the main fraction of the magma erupted during these eruptions. Rhyolitic products range from aphyric, with
237 common xenocrysts of plagioclase and clinopyroxene (i.e. Pietre Cotte lava and pumices, AD 1888-90 eruption bread
238 crust bombs; Piochi et al. 2009; De Astis et al. 2013) to weakly porphyritic (i.e., Pal B pumices). The pumices from the
239 Pal B fallout deposit consist of white lapilli and bombs containing magmatic enclaves and showing a low porphyricity
240 (P.I. is less than 5%) with a glassy groundmass (Fig. 3e). Phenocrysts are, in order of abundance, plagioclase, sanidine,
241 clinopyroxene and biotite. Accessory Ti-magnetite and apatite occur as inclusions within phenocrysts. The latitic and
242 trachytic enclaves are constituted by phenocrysts of plagioclase and clinopyroxene that are surrounded by a dark microlitic
243 matrix (Fig. 3f). The composition of these rhyolites range in SiO₂ from 71 % to 72 wt.% and in Na₂O+K₂O from 9.1 to
244 9.4 wt.% (Table 1; Fig. 2b).

245 246 *4.2 Mineral chemistry of natural products*

247 Plagioclase composition ranges from labradorite to andesine and oligoclase, with a significant overlap for latitic and
248 trachytic products (Fig. 4a; supplementary material). In the latitic enclaves of Pietre Cotte plagioclase is An₃₉₋₅₇Ab<sub>37-
249 48</sub>Or₅₋₁₃, whilst in the Palizzi trachytic lava and in the K-rich trachytic pumices (Pal D) plagioclase is An₃₉₋₆₁Ab₃₄₋₅₀Or₃₋₉

250 and $An_{37-55}Ab_{39-54}Or_{6-13}$, respectively. In contrast, in the rhyolitic pumices (Pal B), plagioclase is $An_{25-59}Ab_{33-66}Or_{3-11}$.
251 Alkali feldspar shows a rather homogeneous composition in all products ($An_{1-6}Ab_{31-44}Or_{51-67}$), with the exception of the
252 K-rich trachytic pumices (Pal D) that are evidently enriched in the Or component ($An_{3-5}Ab_{22-36}Or_{59-72}$).

253 Clinopyroxene has a rather similar augitic composition in all products ($Wo_{42-47}En_{37-42}Fs_{12-19}$), with the Diopside-
254 Hedembergite (DiHd) component ranging from 0.76 to 0.86 (Fig. 5; supplementary material). Clinopyroxene from the
255 K-rich trachytic pumices of Pal D is enriched in the DiHd component (DiHd = 0.83-0.84) with respect to other latitic and
256 trachytic products (DiHd = 0.76-0.82). In the rhyolitic pumices (Pal B), clinopyroxene display a very large compositional
257 variation (DiHd = 0.77-0.86). Biotite in the K-rich trachytic pumices of Pal D has $Mg/(Mg + Fe) = 0.65-0.67$ (Fulignati
258 et al. 2018). Olivine compositions in the latitic and trachytic products varies from Fo_{72} to Fo_{55} (Gioncada et al. 1998).

259 Cores and rims REE patterns in plagioclase reveal that the plagioclase of the K-rich trachytic pumices of Pal D has
260 lower concentrations of HREE with respect to plagioclase of the latitic enclaves of Pietre Cotte and the trachytic lava of
261 Palizzi (Fig. 6a; supplementary material). Sr and Ba abundances in plagioclase are higher in the K-rich trachytic pumices
262 (Pal D) compared to the other latitic and trachytic magmas (Ba up to 2536 ppm and Sr up to 6869 ppm) and show a
263 positive correlation with the Eu anomaly ($Eu/Eu^* = 7-28$, with $Eu^* = (Sm_N - Gd_N)/2 + Gd_N$) (Fig. 6a). Clinopyroxene
264 phenocrysts of Pal D show higher REE concentration compared to clinopyroxene of the latitic enclaves and the trachytic
265 lava of Palizzi (Fig. 6b). The Sr content of clinopyroxene is variable (70-206 ppm), with the lowest values observed for
266 the K-rich trachytic pumices of Pal D and a positive correlation with the Eu anomaly (0.47-0.72) (Fig. 6b; supplementary
267 material).

268 269 4.3 Experimental results

270 Temperature gradient experiments produced variable phase relationships and crystal-melt proportion in response to
271 the temperature variation along the charge (Table 2; Figs. 7-8). In all the experiments, clinopyroxene is the most abundant
272 mineral phase, forming large (200-1000 μm) skeletal crystals in the hotter region of the capsule and small (20-200 μm)
273 and increasingly euhedral crystals at lower temperatures. Such variability of crystal size and shape can be attributed to
274 the effect of undercooling upon cooling from superliquidus (Shea and Hammer 2013; Pontesilli et al. 2019; Masotta et
275 al. 2020). At anhydrous conditions ($H_2O = 0$ wt.%), clinopyroxene is the only mineral in the temperature range 1050-
276 1000 °C. Fe-oxide and alkali feldspar start to crystallize at 1000 °C. The same mineral assemblage constituted by
277 clinopyroxene, Fe-oxide and alkali feldspar is maintained up to the top of the capsule, where the crystal fraction increases
278 up to 80 vol.% at about 900 °C (Table 2; Fig. 8). Upon increasing crystallization, the composition of the interstitial glass
279 enriches in K_2O from 6.0 to 7.3 wt.% with only a slight variation in SiO_2 from 58 to 59 wt.% (Fig. 9; supplementary
280 material). It is worth noting that the glass in the anhydrous experiment is slightly enriched in FeO compared to the starting
281 material, as result of the extensive crystallization of feldspar (Fig. 9). At hydrous conditions with $H_2O = 2$ wt.% and at
282 the temperature of 1050 °C, clinopyroxene and Fe-oxide co-saturate the melt. Biotite crystallization starts at 1000 °C and
283 is followed by the crystallization of plagioclase and alkali feldspar at 925 °C. At the top of the capsule, the temperature
284 decreases to 900 °C and the crystallinity reaches ~50 vol.% (Table 2; Fig. 8). The composition of interstitial glasses along
285 the experimental charge varies with the increasing crystallization, with SiO_2 increasing from 58 to 62 wt.% and K_2O
286 increasing from 5.7 to 6.7 wt.% (Fig. 9; supplementary material). In the higher hydrous experiment with $H_2O = 4$ wt.%,
287 clinopyroxene biotite and Fe-oxide co-saturate the melt in the temperature range 1050-1000 °C and the same mineral
288 assemblage is maintained up until the temperature of 900 °C, where the crystallinity is ~40 vol. % (Table 2; Fig. 8). The
289 composition of interstitial glass varies in SiO_2 from 62 to 67 wt.%, with a rather small increase in K_2O from 5.4 to 6.1
290 wt.% and a marked depletion in FeO, CaO and MgO due to extensive crystallization of biotite and clinopyroxene (Fig. 8;

291 supplementary material).

292

293

294

5. Thermo-barometry and hygrometry

295

296

297

298

299

300

301

302

303

304

305

306

307

308

309

310

311

312

313

314

315

316

317

318

319

320

321

322

323

324

325

326

327

328

329

330

331

332

333

334

335

336

337

338

339

340

341

342

343

344

345

346

347

Crystallization temperature and pressure of products representative of the latitic and trachytic magmas of PCEC (K-rich trachytic pumices of Pal D and trachytic lava flow of Palizzi) and GCEC (latitic enclave of Pietre Cotte lava flow) were estimated using the clinopyroxene-liquid thermo-barometer of Masotta et al. (2013). This model is specific to alkaline differentiated magmas and includes in the calibration dataset experiments performed with the trachytic composition of the Palizzi lava flow. The use of this model theoretically yields to the highest accuracy for the estimates of the intensive variables of magmas erupted at La Fossa (Table 3). Equilibrium clinopyroxene-liquid pairs were selected based on the predicted vs. calculated clinopyroxene DiHd component, assuming at equilibrium the pairs with $\Delta\text{DiHd} < 0.1$ (Mollo and Masotta 2014; Fig. 10a). Most of the clinopyroxene crystals resulted in equilibrium with the latitic and trachytic magmas, with the exception of clinopyroxene in the rhyolitic pumices of Pal B, not used for the calculation of the intensive variables (Fig. 10a). Given the lack of glass in the trachytic lava flow (Palizzi) and the latitic enclave (Pietre Cotte), the bulk rock composition was assumed as representative of the liquid in equilibrium with clinopyroxene. For the K-rich trachytic pumices of Pal D, where the matrix glass was available, we paired crystal cores with the bulk rock and melt inclusion analyses and the crystal rims with matrix glass analyses (data from Fulignati et al. 2018). The H_2O value used as input for the thermo-barometer was assumed between 2.0 and 3.5 wt.%, as determined through iterative solution by combining the plagioclase-liquid hygrometer of Masotta and Mollo (2019) and the clinopyroxene-liquid thermo-barometer of Masotta et al. (2013). We note that to an increase of the H_2O content of 1 wt.% corresponds an increase of the temperature estimates of less than 10 °C.

Pressure and temperature values calculated for the trachytic K-rich Pal D pumices are based on 30 core-liquid pairs and 20 rim-liquid pairs. The cores indicate crystallization temperature and pressure of 1004 ± 14 °C and 160 ± 54 MPa, while crystal rims show slightly lower values of temperature and pressure of 996 ± 13 °C and 132 ± 33 MPa (Fig. 10b). Clinopyroxene core-liquid pairs (20 pairs) from the trachytic lava flow of Palizzi indicate temperature and pressure of 1007 ± 9 °C and 199 ± 39 MPa, whereas rim-liquid pairs (20 pairs) give temperature and pressure of 1005 ± 8 °C and of 208 ± 30 MPa (Fig. 10b). Notably, the estimates obtained using both core and rim analyses are identical within the error. Compared to the trachytic products, the clinopyroxene-liquid pairs of the latitic enclave of Pietre Cotte lava flow indicate higher temperature and pressure, with core-liquid pairs (10 pairs) giving values of 1027 ± 5 °C and 307 ± 47 MPa and rim-liquid pairs (10 pairs) yielding to values of 1025 ± 6 °C and 294 ± 38 MPa (Fig. 10b). As for the trachytic lava of Palizzi, core and rim analyses give results that are identical within the error. Overall, the temperature and pressure distribution inferred using clinopyroxene-liquid thermo-barometry (Fig. 10b) is consistent with the polybaric nature of the plumbing system of La Fossa, with latitic magmas evolving at greater depth compared to trachytic ones.

Further calculation of the crystallization temperatures for the latitic and trachytic magmas at La Fossa have been done using the REE-in-plagioclase-clinopyroxene thermometer (Sun and Liang 2017). This thermometer is based on REE + Y exchange between plagioclase and clinopyroxene. Calculations have been performed assuming pressures of 150 and 300 MPa, and H_2O contents of 2.5 and 3.0 wt.%, for the K-rich trachytic pumices of Pal D and the latitic enclave of Pietre Cotte obsidian, respectively. The results, based on 42 clinopyroxene-plagioclase pairs (14 pairs for each magma composition), indicate average temperatures of 991 ± 31 °C and 1037 ± 8 °C for the Pal D K-rich trachytic pumices and the Pietre Cotte latitic enclave, respectively (Table 3; Figs. 10c-d). These values are consistent with those inferred using the clinopyroxene-liquid thermo-barometer. In contrast, the average temperature obtained for the Palizzi trachytic lava is

332 slightly higher (1057 ± 8 °C), probably testifying to a higher co-saturation temperature for clinopyroxene and plagioclase.

333 Plagioclase-liquid pairs have been used to determine the H₂O content of the K-rich trachytic magma of Pal D eruption,
334 through the plagioclase-liquid hygrometer of Masotta and Mollo (2019). Plagioclase core analyses coupled with the whole
335 rock compositions yield a H₂O content of 2.54 ± 0.57 wt.%, whilst rim analyses coupled with the average composition of
336 the matrix glass indicate a water content of 2.42 ± 0.52 wt.%. These values are in accordance with those proposed for the
337 latitic and trachytic magmas at La Fossa by Masotta and Mollo (2019), and with the highest water content measured in
338 melt inclusions hosted in the Pal D phenocrysts (ranging from 1.01 to 2.52 wt.%, with the low measured values interpreted
339 as degassed hourglass inclusions; Fulignati et al. 2018).

340 The crystallization temperature of the Pal B rhyolite was estimated using the plagioclase-liquid thermometer (Putirka
341 2008), using the plagioclase occurring in the Pal B pumices and the bulk rock analyses as representative of the liquid in
342 equilibrium. Pressures of 100 and 200 MPa were used for calculation, yielding to comparable crystallization temperatures
343 of 952 ± 7 °C and 957 ± 8 °C, respectively (Table 3). All the considered plagioclase-liquid pairs provide values of $K_D(\text{Ab-}$
344 $\text{An})$ of 0.04-0.12, consistent with the equilibrium value of 0.10 ± 0.05 (Putirka 2008). The same plagioclase-liquid pairs,
345 along with the inferred temperatures, have been used in the hygrometer of Masotta and Mollo (2019) to determine the
346 H₂O content of the rhyolitic magma of Pal B pumices, obtaining values of 1.99 ± 0.30 wt.% H₂O.

349 6. Discussion

350 6.1 Magma crystallization conditions

351 A polybaric plumbing system consisting of multiple storage levels with magma batches undergoing mutual
352 interactions has been invoked to explain the broad range of magma composition and the variety of mixing and mingling
353 features observed in the eruptive products at La Fossa volcano (Peccerillo et al. 2006; Piochi et al. 2009; De Astis et al.
354 2013; Paonita et al. 2013; Vetere et al. 2015; Mandarano et al. 2016; Nicotra et al. 2018; Bullock et al. 2019). In spite of
355 the number of studies, a large uncertainty of crystallization pressure and temperature estimates of magmas erupted at La
356 Fossa volcano still exists. This is mostly related to the reduced accuracy of several thermo-barometric models applied to
357 alkaline magma compositions and the lack of equilibrium selection criteria. Indeed, it has been demonstrated that thermo-
358 barometric and hygrometric models that are based on calibration specific to a restricted range of magma compositions
359 have lower uncertainties compared to models based on global regressions (Masotta et al. 2013; Mollo et al. 2015; Perinelli
360 et al. 2016; Brugman and Till 2019). Coherently with previous works, our estimates envisage a polybaric storage system
361 below La Fossa cone but, in addition, they allow to precisely define the difference in the crystallization pressure between
362 the K-rich trachytic magma of Pal D and the other trachytic magmas (Fig. 2b). The K-rich trachytic magma of Pal D
363 pumices equilibrated at a lower pressure (160 ± 54 MPa) compared to other trachytic (208 ± 30 MPa) and latitic (307 ± 47
364 MPa) magmas (Fig. 10b). The lowermost pressure obtained for the K-rich trachytic magma of Pal D (30-50 MPa) is
365 consistent with the minimum H₂O saturation pressure estimated by Fulignati et al. (2018) based on the H₂O content in
366 melt inclusions. We therefore suggest that the K-rich trachytic magma feeding the Pal D eruption was erupted from a
367 reservoir located at shallower depth (1-3 km) compared to those feeding the other latitic and trachytic eruptions (3-8 km).

368 As regarding the rhyolitic magma of Pal B, the inferred temperature of $\sim 955\pm 8$ °C is fully consistent with the
369 temperature estimate of 950 °C inferred for the GCEC rhyolites (Vetere et al. 2015). The lack of clinopyroxene in
370 equilibrium with the rhyolite (Fig. 10a) did not allow a reliable pressure estimate for the rhyolitic magma, however, based
371 on the low H₂O content of the rhyolite (~ 2 wt.%), we can infer a H₂O-saturation pressure below 100 MPa.

372 The crystallization conditions obtained in this study reinforce the evidence of the capability of the shallow magma

373 system of La Fossa to feed also significant explosive eruptions. Indeed, the rhyolitic Pal B and K-rich trachytic Pal D
374 eruptions constitute the main explosive events occurred at La Fossa volcano during the studied period, being characterized
375 by similar plume height (7-8 km a.s.l.) and erupted volume ($3.6-4.0 \times 10^6 \text{ m}^3$) (Biass et al. 2016).

376 377 *6.2 Magma differentiation modelling*

378 One of the most interesting features at la Fossa volcano is the twofold differentiation path followed by intermediate
379 magmas during their late evolution, leading to the formation of either K-rich trachytes (represented by Pal D pumices) or
380 trachytes (the trachytic lava flows of Palizzi, Punte Nere and Campo Sportivo) and then rhyolites (represented by the
381 obsidian lava flows of Commenda and Pietre Cotte or by the pumices of Pal B) (Fig. 2b). A combination of fractional
382 crystallization and crustal assimilation (AFC) processes has been invoked in order to explain the formation of the rhyolitic
383 magmas starting from the less differentiated latitic ones (Clocchiatti et al. 1994; Del Moro et al. 1998; Piochi et al. 2009;
384 Pinarelli et al. 2019; Bullock et al. 2019). The low content of Ba and Sr, and the negative Eu anomaly of the Pietre Cotte
385 rhyolitic lava testifies to a process of fractional crystallization with a significant involvement of plagioclase and K-
386 feldspar (Piochi et al. 2009). In this framework, we explored what processes determined the enrichment in K_2O that
387 produced the K-rich trachytic magma and the differentiation to trachytes and rhyolites. We thus performed mass balance
388 calculations using major element composition of bulk rocks and minerals, starting from the latitic magma (latitic enclave
389 of Pietre Cotte obsidian) and targeting the composition of both the trachytic (i.e., the K-rich trachyte of Pal D pumices
390 and the trachyte of the Palizzi lava) and the rhyolitic (i.e, Pal B pumice) magmas. The choice of the latite as starting point
391 for the differentiation modelling is supported by the fact that this composition represents: i) one of the least evolved
392 intermediate magma erupted at La Fossa and ii) the point in the differentiation line where two distinct evolutionary trends
393 branch out (Figs. 2b). Four possible differentiation segments are thus modelled (Fig. 11):

- 394
395 1. *Latite to K-rich trachyte*: the K-rich trachytic composition of Pal D pumices is obtained through fractionation
396 (~31%) of a mineral assemblage made up by plagioclase (17%), clinopyroxene (7%), sanidine (4%), Fe-Ti oxide (2%),
397 olivine (1%) and biotite (0.5%).
- 398 2. *Latite to trachyte*: the trachytic composition of the Palizzi lava is obtained through fractionation (~38%) of a mineral
399 assemblage made up by sanidine (14%), plagioclase (13%), clinopyroxene (5%), biotite (1%), Fe-Ti oxide (3%) and
400 olivine (~1%).
- 401 3. *K-rich trachyte to rhyolite*: the rhyolitic composition of Pal B pumices is obtained through fractionation (~68%) of
402 a mineral assemblage made up by sanidine (39%), plagioclase (19%), biotite (6%), Fe-Ti oxide (4%) and clinopyroxene
403 (1%).
- 404 4. *Trachyte to rhyolite*: the rhyolitic composition of Pal B pumices is obtained through fractionation of a mineral
405 assemblage (~62%) made up by sanidine (26%), plagioclase (24%), clinopyroxene (5%), Fe-Ti oxide (4%) and biotite
406 (3%).

407
408 Concerning the differentiation toward the two trachytic terms (hereafter referred to K-rich and normal trachytes),
409 segments 1 and 2 differ substantially in the proportions of fractionated mineral phases. The plagioclase/sandine ratio
410 varies from about 4:1 to about 1:1, determining the evolution of the melt toward either K-rich (segment 1) or normal
411 (segment 2) trachytes (Fig. 11). The two contrasting trends can be associated to the different pressures inferred from
412 thermo-barometric calculation, suggesting a lower pressure for the K-rich trachyte compared to normal trachyte. Indeed,
413 the higher fractionation of plagioclase would be favored at a lower pressure due to the lower activity of H_2O in the melt.

414 This is supported by the higher Eu anomaly and Sr concentration of plagioclase in the K-rich trachytes of Pal D pumices
415 compared to plagioclase of the Palizzi lava trachyte (Fig. 6a). The formation of the rhyolite has been modelled by
416 considering differentiation paths starting from both K-rich and normal trachytes (segments 3 and 4, respectively; Fig. 11).
417 Segment 3 differs from segment 4 because of the higher plagioclase/sanidine ratio (about 2:1 against about 1:1) and the
418 higher biotite/clinopyroxene ratio (about 6:1 against about 1:2). The compositional variability of magmas erupted at La
419 Fossa (Fig. 2b), with the K-rich trachytic composition being observed only in a single eruptive event (Pal D pumices),
420 overall suggests that rhyolitic magmas originated through differentiation of normal trachytes. This is supported by the
421 lack of solid enclaves enriched in biotite with respect to clinopyroxene and by the higher pressure estimates for the normal
422 trachytes, compared to the K-rich one.

423 In addition to the mass balance calculations using major elements, we modelled the evolution of latitic and trachytic
424 magmas using assimilation+fractional crystallization (AFC) trace elements modelling (see supplementary material for
425 the used parameters). Some extent of crustal assimilation has been invoked to explain the complex evolution of magmas
426 erupted at La Fossa volcano, through the interaction with crustal rock of the Calabro Peloritano basement (Frezzotti et al.
427 2004; Piochi et al. 2009; De Astis et al. 2013). Hence, starting from the same latitic composition and assuming the same
428 phase assemblage obtained through mass balance calculations, the formation of the rhyolitic magma (Pal B pumices) is
429 entirely explained by 50 to 60% crystal fractionation with an assimilation rate between 0.2 and 0.5 (Fig. 12). This
430 calculation also shows that the trachytic products are better explained by low degrees of fractional crystallization, whilst
431 assimilation becomes increasingly important during the late evolution to rhyolites, as suggested by Del Moro et al. (1998).
432 In contrast, the origin of the K-rich trachytic magma is explained by 30 to 40% crystal fractionation involving a higher
433 plagioclase/sanidine ratio in the fractionated solid and leading to an increase in Ba (Fig. 12).

434 Temperature gradient experiments explored the effect of the H₂O content (0, 2 and 4 wt.%) on the differentiation of
435 the latitic magma, designating different paths of melt differentiation that overall indicate an increase of the SiO₂/K₂O
436 ratio with the increasing H₂O in the system (Fig. 9). The interstitial glasses analyzed in the two experiments with 0 and 2
437 wt.% H₂O better approximate the K₂O enrichment trend modelled by segment 1 (K-rich trachytes), whereas the most
438 hydrous experiment with 4 wt.% H₂O approximates the SiO₂ enrichment trend modelled by segments 2 and 4 (trachytes
439 and rhyolites). Overall, the divergence of these trends is explained by the different proportion of feldspars, clinopyroxene
440 and biotite that crystallize at different H₂O content (see Table 2). Therefore, in ultimate analysis, experimental results
441 confirm what inferred from the differentiation modelling and from thermo-barometric analyses, that the K-rich trachytic
442 magma of Pal D originated at lower pressure and at lower H₂O concentration compared to other trachytic magmas erupted
443 at La Fossa volcano. More than other parameters, the H₂O content in the melt (in turn related to the storage depth of the
444 magma), by varying the clinopyroxene/feldspar+biotite ratio, exerts a primary control on phase stability and determines
445 the differentiation trend towards either K-rich trachytes (segment 1) or trachytes and rhyolites (segments 2 and 4). The
446 higher H₂O content of both latitic and trachytic magmas, compared to the K-rich trachytic one, is in accordance with the
447 H₂O estimates of 2.5-3.5 wt.% inferred using the plagioclase-liquid hygrometer (Masotta and Mollo 2019). This finding
448 is in accordance with experimental results by Beermann et al. (2017), reproducing the crystallization of basaltic andesite
449 of the 24 ka Lower Pollara eruption (Salina, Aeolian Islands) and demonstrating that a strong increase of K₂O relative to
450 SiO₂ can be reproduced at higher temperatures and relatively low H₂O content.

6.3 The role of crystal mushes within La Fossa plumbing system

451
452
453 Using mass balance calculations and AFC modelling on major and trace elements, we showed that rhyolitic magmas
454 are produced from an initial latitic composition by a minimum of 60% of crystal fractionation (Figs. 11 and 12). The low

455 porphyritic or even aphyric nature of the rhyolitic magmas erupted at La Fossa **is in contrast with this result** and other
456 possibilities regarding the formation of crystal-poor differentiated magmas must be considered.

457 The origin of the crystal-poor rhyolites by partial melting of subvolcanic rocks favored by the intrusion of hotter
458 magmas at depth, as proposed by Masotta et al. (2018) for the formation of rhyolitic melts at Krafla volcano (Iceland),
459 can be ruled out, since the lithology of the subvolcanic rocks are inconsistent with the formation of rhyolitic melts. The
460 perforations carried out for geothermal exploration within the La Fossa Caldera at 1000 m and 2000 m revealed the
461 presence of latitic-shoshonitic subvolcanic bodies, as well as a monzogabbroic body (Faraone et al. 1986; Gioncada and
462 Sbrana 1991), which could be consistent with the variety of enclaves contained in the rhyolitic products but not with the
463 origin of the rhyolite itself. The rather homogeneous composition of the rhyolitic magmas erupted at La Fossa in the last
464 1000 years contrasts with the heterogeneity of the lithotypes revealed by the perforations. Moreover, partial melting of
465 latitic and trachytic lithologies is inconsistent with the low content of Ba, Sr and the high Eu anomaly that, in turn, are
466 better explained by processes of crystal fractionation plus a small amount of crustal assimilation (Fig. 12).

467 As alternative to partial melting of shallow crustal rocks, the crystal-poor rhyolite could be explained in the light of
468 efficient crystal-melt separation processes. It is widely accepted that the architecture of magmatic system, also those
469 belonging to arc settings, should be envisaged in a “mush-dominating” perspective, where the melts and exsolved fluids
470 are distributed within a crystalline network, in vertically developed systems (Cashman et al. 2017; Edmonds et al. 2019;
471 Sparks et al. 2019). In this scenario, crystal-poor melts with evolved composition can be generated by the extraction from
472 crystal mushes of intermediate composition **favored by efficient crystal-melt separation processes**. **These** models include:
473 i) compaction-induced segregation of melt and subsequent extrusion of interstitial melt in response to deformation and
474 settling of a crystalline framework (Bachmann and Bergantz 2004), ii) segregation of evolved liquid **induced by**
475 **gravitational instability of the upper solidification front** (Marsh 2002; Masotta et al. 2012b) **and iii) filter-press induced**
476 **by volatile exsolution** (Pistone et al. 2015). Thermo-mechanical modelling suggests that melt extraction is more efficient
477 at high crystal content between 50 and 70% (Dufek and Bachmann 2010). In this context, volatile exsolution plays a
478 fundamental role on the physical and rheological properties of melt **produced within mush-dominated** regions of such
479 systems (Parmigiani et al. 2014; Edmonds et al. 2019). When the fluid exsolution is reached, in a system largely
480 dominated by a high crystal fraction (50-70%), the volatile phase is concentrated in narrow channels (Oppenheimer et al.
481 2015) **that may favor** the segregation of melt locked in the crystal network through gas-driven filter pressing (Sisson et
482 al. 1999; Pistone et al. 2015). A similar process was also observed in temperature gradient experiments by Rodriguez et
483 al. (2017), who described the migration through the crystal mush of a fluid phase exsolved in it through second boiling
484 (i.e. volatile exsolution induced by isobaric crystallization). At La Fossa volcano, pre-eruptive volatile exsolution is likely
485 to occur at the rhyolite stage in the shallow system (Gioncada et al. 1998; Fulignati et al. 2018). Following these
486 considerations, we suggest that rhyolitic magmas at La Fossa could be generated by **AFC processes** within crystal mushes,
487 being eventually extracted favored by the exsolved fluid phase. **The effects of the fluid phase are twofold as they**
488 **contribute in: i) rejuvenating the crystal mush through the increase of the melt fraction** (Pistone et al. 2017) **and ii)**
489 **decreasing the melt viscosity, in turn favoring the melt extraction from the crystal mush** (Ardia et al. 2008; Pistone et al.
490 2013). These processes can be even more effective in the case of a mush system that approaches the second boiling upon
491 late solidification (Edmonds et al. 2019). In this framework, the volcanic unrests occurred between AD 1977-1999 and
492 in AD 2004 culminated, only in an intensification of the fumarolic temperatures and in changes of the chemical
493 compositions of the **gases discharged, were possibly caused by the second boiling of the intermediate mushy magmas,**
494 **not followed by remobilization of the interstitial melt**. Indeed, the changes in the fumarolic activity have not been
495 accompanied by deep seismicity and ground deformation, suggesting that no movement of magma occurred at shallow

496 levels (Granieri et al. 2006; Paonita et al. 2013).

497 If we assume that the latitic-trachytic magmas represent the closest parental compositions from which the rhyolitic
498 magma originated, it is important to consider the genetic relationship between the rhyolite and the latitic-trachytic
499 enclaves. In the similar context of Lipari island, Davì et al. (2010) demonstrated that the rhyolitic magma feeding the
500 Rocche Rosse lava flow was produced through AFC processes, starting from the latitic magma compositions represented
501 by magmatic enclaves contained in the rhyolitic lava. These enclaves, according to Forni et al. (2015), represent
502 remobilized and partially melted portions of the crystal mush from which the rhyolitic melt originated. In a similar fashion,
503 the coexistence of latitic-trachytic and rhyolitic magmas in the eruptive products of La Fossa testifies to the presence of
504 magmas belonging to the same liquid line of descent, but yielding to different types of interaction. The contrasting
505 rheological behavior of the crystal-rich latitic-trachytic enclaves and the host rhyolitic magma, as in the case of the Pietre
506 Cotte obsidian, suggests that very different rheology characterized the two magma domains (i.e., the enclaves were
507 entrained in a nearly solid state; P.I. = 25-30%). In contrast, in the case of mingled products of Pietre Cotte pumices and
508 the Commenda lava, the trachytic-latitic domain had similar rheological behavior. Consistently, the crystal content of the
509 latitic-trachytic domain (P.I. ranging from 3 to 30%) overlaps only in part the crystallinity range that defines the magma
510 as a crystal mush (25-50%; Marsh 1996) and that in turn allows to classify the magmatic enclaves of Pietre Cotte as
511 remobilized fragments of the crystal mush (Fig. 13).

512 The remobilization of the crystal mush could have been favored by the arrival of a new batch of hotter (latitic) magma.
513 Assuming that part of this magma was also erupted (e.g. evidence for the eruption of a latitic magma is the banding in the
514 Pietre Cotte pumices and Commenda lava), the remaining part interacted with the crystal mush at depth. The melting of
515 lower temperature phases such as alkali feldspar and biotite, almost absent in magmatic enclaves, but necessary to form
516 rhyolitic magma (see section 6.2), reduced the crystallinity and promoted the hydration and remobilization of the crystal
517 mush. The previously extracted rhyolitic melt and the remobilized portions of the crystal mush (i.e., enclaves and
518 glomerocrysts) are thus erupted together (Fig. 13). This is also evident in the geochemical characteristics of the magmatic
519 enclaves of Pietre Cotte, where high-Sr plagioclase (Piochi et al. 2009) is often surrounded by an overgrowth of sanidine,
520 related to the crystallization from a melt originated by partial melting of a feldspar-rich crystal mush (Forni et al. 2015).
521 The overall texture of magmatic enclaves and, more in general, of the lati-trachytic magmas that exhibit a broad range of
522 crystal size, shape and textures (including glomerocrysts; Figs. 3a-b) supports this hypothesis. This variability may be
523 caused not only by the repeated episodes of mafic recharge, magma ascent and mixing in short time scales (1-10 years,
524 Nicotra et al. 2018), but also by the variable degree of interaction of the mafic magmas with the crystal mushes.

526 7. Concluding remarks

527 The complex relationships among latitic, trachytic and rhyolitic magmas erupted at La Fossa volcano in the last 1000
528 years are unveiled by mineral-liquid thermo-barometry and hygrometry, geochemical modelling and temperature
529 gradient experiments. By combining these information with the petrographic analysis of explosive and effusive products,
530 a new model of the polybaric magmatic system is obtained and the following conclusions can be drawn:

- 531 - the latitic magma represents the least differentiated composition erupted at La Fossa volcano in the last 1000
532 years and the closest parental magma for both K-rich (Pal D) and normal trachytes (Palizzi lava flow);
- 533 - the K-rich trachytic magma of Pal D originated at lower depth (corresponding to 160 ± 54 MPa) and less hydrous
534 conditions compared to normal trachytic magmas (208 ± 30 MPa);
- 535 - the rhyolitic melt originated within the latitic-trachytic crystal mush and eventually segregated into crystal-poor
536 batches, upon increased volatile concentration in the fluid phase (i.e. second boiling of mushy magmas), through gas filter

62
63
64
65

537 pressing process;
538 - latitic and trachytic enclaves and mingled bands in rhyolites, as well as glomerocrysts, testify to disrupted
539 portions of the crystal mush (i.e. highly porphyritic enclaves) and the mafic (latitic) magma responsible for the mush
540 remobilization.

541

542 **Acknowledgments**

543 The authors thank the editor and the two anonymous reviewers for their valuable comments, A. Risplendente
544 (Università di Milano), O. Bruguier (Université de Montpellier), R. Ishak (Università di Pisa) for assistance during
545 analytical work, F. Colarieti and M. Gemelli (Università di Pisa) for samples preparation. The research was funded by
546 Università di Pisa “FFABR - Ricerca di Base” to AG, “FFABR - Ricerca di Base” and “PRA 2018 - Progetti di Ricerca
547 di Ateneo” to MM and MP and by the Italian Ministero dell'Istruzione, dell'Università e della Ricerca (MIUR) through
548 the Progetti di Rilevante Interesse Nazionale (PRIN) "Time scales of solidification in magmas: Applications to Volcanic
549 Eruptions, Silicate Melts, Glasses, Glass-Ceramics” project (PRIN2017J277S9) to MM. This research is part of SC PhD
550 program funded by a Tuscany Regional “Pegaso” doctoral grant.

551

552 **References**

- 553 Ardia P, Giordano D, Schmidt MW (2008) A model for the viscosity of rhyolite as a function of H₂O-content and pressure:
554 A calibration based on centrifuge piston cylinder experiments. *Geochimica et Cosmochimica Acta*, 72(24), 6103-
555 6123
- 556
- 557 Bachmann O, Bergantz GW (2004) On the origin of crystal-poor rhyolites: extracted from batholithic crystal
558 mushes. *Journal of Petrology*, 45(8), 1565-1582
- 559
- 560 Beermann O, Holtz F, Duesterhoeft E (2017) Magma storage conditions and differentiation of the mafic Lower Pollara
561 volcanics, Salina Island, Aeolian Islands, Italy: implications for the formation conditions of shoshonites and
562 potassic rocks. *Contributions to Mineralogy and Petrology*, 172(5), 37
- 563
- 564 Biass S, Bonadonna C, Di Traglia F, Pistolesi M, Rosi M, Lestuzzi P (2016) Probabilistic evaluation of the physical
565 impact of future tephra fallout events for the Island of Vulcano, Italy. *Bulletin of Volcanology*, 78(5), 37
- 566
- 567 Brugman KK, Till CB (2019) A low-aluminum clinopyroxene-liquid geothermometer for high-silica magmatic
568 systems. *American Mineralogist*, 104(7), 996-1004
- 569
- 570 Bullock LA, Gertisser R, O'Driscoll B, Harland S (2019) Magmatic evolution and textural development of the 1739 CE
571 Pietre Cotte lava flow, Vulcano, Italy. *Journal of Volcanology and Geothermal Research*, 372, 1-23
- 572
- 573 Cashman KV, Sparks RSJ, Blundy JD (2017) Vertically extensive and unstable magmatic systems: a unified view of
574 igneous processes. *Science* 355(6331), eaag3055
- 575
- 576 Cioni R, Marianelli P, Santacroce R (1998) Thermal and compositional evolution of the shallow magma chambers of
577 Vesuvius: evidence from pyroxene phenocrysts and melt inclusions. *Journal of Geophysical Research: Solid
578 Earth*, 103(B8), 18277-18294

579

580

581

582

583

578
579
580
581
582
583
584
585
586
587
588
589
590
591
592
593
594
595
596
597
598
599
600
601
602
603
604
605
606
607
608
609
610
611
612
613
614
615
616
617
618
62
63
64
65

Clocchiatti R, Del Moro A, Gioncada A, Joron JL, Mosbah M, Pinarelli L, Sbrana A (1994) Assessment of a shallow magmatic system: the 1888–90 eruption, Vulcano Island, Italy. *Bulletin of Volcanology*, 56(6-7), 466-486

Davì M, De Rosa R, Donato P, Vetere F, Barca D, Cavallo A (2009) Magmatic Evolution and plumbing system of ring-fault volcanism: the Vulcanello Peninsula (Aeolian Islands, Italy). *European Journal of Mineralogy*, 21(5), 1009-1028

Davì M, De Rosa R, Holtz F (2010) Mafic enclaves in the rhyolitic products of Lipari historical eruptions; relationships with the coeval Vulcano magmas (Aeolian Islands, Italy). *Bulletin of volcanology*, 72(8), 991-1008

De Astis G, La Volpe L, Peccerillo A, Civetta L (1997) Volcanological and petrological evolution of Vulcano island (Aeolian Arc, southern Tyrrhenian Sea). *Journal of Geophysical Research: Solid Earth*, 102(B4), 8021-8050

De Astis G, Lucchi F, Dellino P, La Volpe L, Tranne CA, Frezzotti, ML, Peccerillo A (2013) Geology, volcanic history and petrology of Vulcano (central Aeolian archipelago). *Geological Society, London, Memoirs*, 37(1), 281-349

De Fino M, La Volpe L, Piccarreta G (1991) Role of magma mixing during the recent activity of La Fossa di Vulcano (Aeolian Islands, Italy). *Journal of volcanology and geothermal research*, 48(3-4), 385-398

Del Moro A, Gioncada A, Pinarelli L, Sbrana A, Joron JL (1998) Sr, Nd, and Pb isotope evidence for open system evolution at Vulcano, Aeolian Arc, Italy. *Lithos*, 43(2), 81-106

Di Traglia F, Pistolesi M, Rosi M, Bonadonna C, Fusillo R, Roverato M (2013) Growth and erosion: The volcanic geology and morphological evolution of La Fossa (Island of Vulcano, Southern Italy) in the last 1000 years. *Geomorphology*, 194, 94-107

Dufek J, Bachmann O (2010) Quantum magmatism: Magmatic compositional gaps generated by melt-crystal dynamics. *Geology*, 38(8), 687-690

Edmonds M, Cashman KV, Holness M, Jackson M (2019) Architecture and dynamics of magma reservoirs. Architecture and dynamics of magma reservoirs. *Philosophical Transactions of the Royal Society A*, 377

Faraone D, Silvano A, Verdiani G (1986) The monzogabbroic intrusion in the island of Vulcano, Aeolian Archipelago, Italy. *Bulletin of volcanology*, 48(5), 299-307

Forni F, Ellis BS, Bachmann O, Lucchi F, Tranne CA, Agostini S, Dallai L (2015) Erupted cumulate fragments in rhyolites from Lipari (Aeolian Islands). *Contributions to Mineralogy and Petrology*, 170(5-6), 49

Frazzetta G, La Volpe L, Sheridan MF (1983) Evolution of the Fossa cone, Vulcano. *Journal of Volcanology and Geothermal Research*, 17(1-4), 329-360

619
620
2
621
622
5
623
624
8
625
626
10
11
627
12
628
14
629
16
630
17
631
19
632
20
633
22
634
23
635
25
636
26
637
28
638
29
639
31
640
32
641
34
642
35
643
37
644
38
645
40
646
42
647
43
648
45
649
46
650
48
651
49
652
51
653
52
654
54
655
55
656
57
657
58
658
60
659
61
62
63
64
65

- Frezzotti ML, Peccerillo A, Zanon V, Nikogosian I (2004) Silica-rich melts in quartz xenoliths from Vulcano Island and their bearing on processes of crustal anatexis and crust–magma interaction beneath the Aeolian Arc, Southern Italy. *Journal of petrology*, 45(1), 3-26
- Fusillo R, Di Traglia F, Gioncada A, Pistolesi M, Wallace PJ, Rosi M (2015) Deciphering post-caldera volcanism: insight into the Vulcanello (Island of Vulcano, Southern Italy) eruptive activity based on geological and petrological constraints. *Bulletin of Volcanology*, 77(9), 76
- Fulignati P, Gioncada A, Costa S, Di Genova D, Di Traglia F, Pistolesi M (2018) Magmatic sulfide immiscibility at an active magmatic-hydrothermal system: The case of La Fossa (Vulcano, Italy). *Journal of Volcanology and Geothermal Research*, 358, 45-57
- Gioncada A, Clocchiatti R, Sbrana A, Bottazzi P, Massare D, Ottolini L (1998) A study of melt inclusions at Vulcano (Aeolian Islands, Italy): insights on the primitive magmas and on the volcanic feeding system. *Bulletin of Volcanology*, 60(4), 286-306
- Gioncada A, Sbrana A (1991) “La Fossa caldera”, Vulcano: inferences from deep drillings. *Acta Vulcanologica*. 1, 115-126
- Granieri D, Carapezza ML, Chiodini G, Avino R, Caliro S, Ranaldi M, Tarchini L (2006) Correlated increase in CO₂ fumarolic content and diffuse emission from La Fossa crater (Vulcano, Italy): *Evidence of volcanic unrest or increasing gas release from a stationary deep magma body?*. *Geophysical Research Letters*, 33(13)
- Gurioli L, Zanella E, Gioncada A, Sbrana A (2012) The historic magmatic-hydrothermal eruption of the Breccia di Commenda, Vulcano, Italy. *Bulletin of volcanology*, 74(5), 1235-1254
- Huang F, Lundstrom CC, Glessner J, Ianno A, Boudreau A, Li J, Ferréc EC, Marshaka S, DeFrates J (2009) Chemical and isotopic fractionation of wet andesite in a temperature gradient: experiments and models suggesting a new mechanism of magma differentiation. *Geochimica et Cosmochimica Acta*, 73(3), 729-749
- Keller J (1980) The island of Vulcano. *Rendiconti della società Italiana di Mineralogia e Petrologia*, 36, 368-413
- Laumonier M, Laporte D, Faure F, Provost A, Schiano P, Ito K (2019) An experimental study of dissolution and precipitation of forsterite in a thermal gradient: implications for cellular growth of olivine phenocrysts in basalt and melt inclusion formation. *Contributions to Mineralogy and Petrology*, 174(11), 94
- Mandarano M, Paonita A, Martelli M, Viccaro M, Nicotra E, Millar IL (2016) Revealing magma degassing below closed-conduit active volcanoes: geochemical features of volcanic rocks versus fumarolic fluids at Vulcano (Aeolian Islands, Italy). *Lithos*, 248, 272-287
- Marsh BD (1996) Solidification fronts and magmatic evolution. *Mineralogical Magazine*, 60(398), 5-40

660
661
662
663
664
665
666
667
668
669
670
671
672
673
674
675
676
677
678
679
680
681
682
683
684
685
686
687
688
689
690
691
692
693
694
695
696
697
698
699
700
701
702
703
704
705

Marsh BD (2002) On bimodal differentiation by solidification front instability in basaltic magmas, part 1: basic mechanics. *Geochimica et Cosmochimica Acta*, 66(12), 2211-2229

Masotta M, Freda C, Paul TA, Moore GM, Gaeta M, Scarlato P, Troll VR (2012a) Low pressure experiments in piston cylinder apparatus: calibration of newly designed 25 mm furnace assemblies to P= 150 MPa. *Chemical geology*, 312, 74-79

Masotta M, Freda C, Gaeta M (2012b) Origin of crystal-poor, differentiated magmas: insights from thermal gradient experiments. *Contributions to Mineralogy and Petrology*, 163(1), 49-65

Masotta M, Mollo S, Freda C, Gaeta M, Moore G (2013) Clinopyroxene–liquid thermometers and barometers specific to alkaline differentiated magmas. *Contributions to Mineralogy and Petrology*, 166(6), 1545-1561

Masotta M, Mollo S, Nazzari M, Tecchiato V, Scarlato P, Papale P, Bachmann O (2018) Crystallization and partial melting of rhyolite and felsite rocks at Krafla volcano: A comparative approach based on mineral and glass chemistry of natural and experimental products. *Chemical Geology*, 483, 603-618

Masotta M, Mollo S (2019) A New Plagioclase-Liquid Hygrometer Specific to Trachytic Systems. *Minerals*, 9(6), 375

Masotta M, Pontesilli A, Mollo S, Armienti P, Ubide T, Nazzari M, Scarlato P (2020) The role of undercooling during clinopyroxene growth in trachybasaltic magmas: Insights on magma decompression and cooling at Mt. Etna volcano. *Geochimica et Cosmochimica Acta*, 268, 258-276

Mollo S, Masotta M (2014) Optimizing pre-eruptive temperature estimates in thermally and chemically zoned magma chambers. *Chemical Geology*, 368, 97-103

Mollo S, Masotta M, Forni F, Bachmann O, De Astis G, Moore G, Scarlato P (2015) A K-feldspar–liquid hygrometer specific to alkaline differentiated magmas. *Chemical Geology*, 392, 1-8

Neri A, Aspinall WP, Cioni R, Bertagnini A, Baxter PJ, Zuccaro G, Hincks TK (2008) Developing an event tree for probabilistic hazard and risk assessment at Vesuvius. *Journal of volcanology and geothermal research*, 178(3), 397-415

Nicotra E, Giuffrida M, Viccaro M, Donato P, D'Orlando C, Paonita A, De Rosa R (2018) Timescales of pre-eruptive magmatic processes at Vulcano (Aeolian Islands, Italy) during the last 1000 years. *Lithos*, 316, 347-365

Oppenheimer J, Rust AC, Cashman KV, Sandnes B (2015) Gas migration regimes and outgassing in particle-rich suspensions. *Frontiers in Physics*, 3, 60

Paonita A, Federico C, Bonfanti P, Capasso G, Inguaggiato S, Italiano F, Sortino F (2013) The episodic and abrupt geochemical changes at La Fossa fumaroles (Vulcano Island, Italy) and related constraints on the dynamics,

- 701 structure, and compositions of the magmatic system. *Geochimica et cosmochimica acta*, 120, 158-178
- ~~702~~
- ~~703~~ 2 Parmigiani A, Huber C, Bachmann O (2014) Mush microphysics and the reactivation of crystal- rich magma
704 reservoirs. *Journal of Geophysical Research: Solid Earth*, 119(8), 6308-6322
- ~~705~~ 5
- 706 Peccerillo A, Frezzotti ML, De Astis G, Ventura G (2006) Modeling the magma plumbing system of Vulcano (Aeolian
707 Islands, Italy) by integrated fluid-inclusion geobarometry, petrology, and geophysics. *Geology*, 34(1), 17-20
- ~~708~~ 8
- ~~709~~ 11 Perinelli C, Mollo S, Gaeta M, De Cristofaro SP, Palladino DM, Armienti P, Putirka KD (2016) An improved
710 clinopyroxene-based hygrometer for Etnean magmas and implications for eruption triggering
711 mechanisms. *American Mineralogist*, 101(12), 2774-2777
- ~~712~~ 14
- ~~713~~ 17 Perugini D, Valentini L, Poli G (2007) Insights into magma chamber processes from the analysis of size distribution of
714 enclaves in lava flows: A case study from Vulcano Island (Southern Italy). *Journal of Volcanology and Geothermal
715 Research*, 166(3-4), 193-203
- ~~716~~ 20
- ~~717~~ 23 Pinarelli L, Gioncada A, Capaccioni B, Vaselli O, Downes H (2019) Mantle source heterogeneity in subduction zones:
718 constraints from elemental and isotope (Sr, Nd, and Pb) data on Vulcano Island, Aeolian Archipelago,
719 Italy. *Mineralogy and Petrology*, 113(1), 39-60
- ~~720~~ 25
- ~~721~~ 26 Piochi M, De Astis G, Petrelli M, Ventura G, Sulpizio R, Zanetti A (2009) Constraining the recent plumbing system of
722 Vulcano (Aeolian Arc, Italy) by textural, petrological, and fractal analysis: the 1739 AD Pietre Cotte lava
723 flow. *Geochemistry, Geophysics, Geosystems*, 10(1)
- ~~724~~ 28
- ~~725~~ 29 Pistone M, Arzilli F, Dobson KJ, Cordonnier B, Reusser E, Ulmer P, Blundy JD (2015) Gas-driven filter pressing in
726 magmas: Insights into in-situ melt segregation from crystal mushes. *Geology*, 43(8), 699-702
- ~~727~~ 31
- ~~728~~ 32 Pistone M, Blundy J, Brooker RA (2017) Water transfer during magma mixing events: Insights into crystal mush
729 rejuvenation and melt extraction processes. *American Mineralogist*, 102(4), 766-776
- ~~730~~ 34
- ~~731~~ 35 Pistone M, Caricchi L, Ulmer P, Reusser E, Ardia P (2013) Rheology of volatile-bearing crystal mushes: mobilization
732 vs. viscous death. *Chemical Geology*, 345, 16-39
- ~~733~~ 37
- ~~734~~ 38 Pistone M, Masotta M, Nazzari M, Mollo S, Armienti P, Scarlato P, Brenna M (2019) Crystallization kinetics of
735 clinopyroxene and titanomagnetite growing from a trachybasaltic melt: New insights from isothermal time-series
736 experiments. *Chemical Geology*, 510, 113-129
- ~~737~~ 40
- ~~738~~ 41 Putirka KD (2008) Thermometers and barometers for volcanic systems. *Reviews in mineralogy and geochemistry*, 69(1),
739 61-120
- ~~740~~ 43
- ~~741~~ 44 Rodríguez C, Castro A (2017) Silicic magma differentiation in ascent conduits. Experimental constraints. *Lithos*, 272,
742 261-277
- ~~743~~ 46
- ~~744~~ 48
- ~~745~~ 49
- ~~746~~ 51
- ~~747~~ 52
- ~~748~~ 53
- ~~749~~ 54
- ~~750~~ 55
- ~~751~~ 56
- ~~752~~ 57
- ~~753~~ 58
- ~~754~~ 59
- ~~755~~ 60
- ~~756~~ 61
- ~~757~~ 62
- ~~758~~ 63
- ~~759~~ 64
- ~~760~~ 65

742
743
744
745
746
747
748
749
750
751
752
753
754
755
756
757
758
759
760
761
762
763
764
765
766
767
768
769
770
771
772
773
774
775
776
777
778
779
780
781
782
62
63
64
65

Rodríguez C, Geyer A, Castro A, Villaseñor A (2015) Natural equivalents of thermal gradient experiments. *Journal of Volcanology and Geothermal Research* 298, 47-58

Rosi M, Di Traglia F, Pistolesi M, Ongaro TE, Vitturi MDM, Bonadonna C (2018) Dynamics of shallow hydrothermal eruptions: new insights from Vulcano's Breccia di Commenda eruption. *Bulletin of Volcanology*, 80(12), 83

Rossi S, Petrelli M, Morgavi D, Vetere F, Almeev RR, Astbury RL, Perugini D (2019) Role of magma mixing in the pre-eruptive dynamics of the Aeolian Islands volcanoes (Southern Tyrrhenian Sea, Italy). *Lithos*, 324, 165-179

Scaillet B, Pichavant M, Cioni R (2008) Upward migration of Vesuvius magma chamber over the past 20,000 years. *Nature*, 455(7210), 216

Shea T, Hammer JE (2013) Kinetics of cooling-and decompression-induced crystallization in hydrous mafic-intermediate magmas. *Journal of Volcanology and Geothermal research*, 260, 127-145

Sisson TW, Bacon CR (1999) Gas-driven filter pressing in magmas. *Geology*, 27(7), 613-616

Sparks RSJ, Annen C, Blundy JD, Cashman KV, Rust AC, Jackson MD (2019) Formation and dynamics of magma reservoirs. *Philosophical Transactions of the Royal Society A*, 377(2139), 20180019

Sun C, Liang Y (2017) A REE-in-plagioclase–clinopyroxene thermometer for crustal rocks. *Contributions to Mineralogy and Petrology*, 172(4), 24

Vetere F, Petrelli M, Morgavi D, Perugini D (2015) Dynamics and time evolution of a shallow plumbing system: the 1739 and 1888-90 eruptions, Vulcano Island, Italy. *Journal of Volcanology and Geothermal Research*, 306, 74-82

Zanon V, Frezzotti ML, Peccerillo A (2003) Magmatic feeding system and crustal magma accumulation beneath Vulcano Island (Italy): evidence from CO₂ fluid inclusions in quartz xenoliths. *Journal of Geophysical Research: Solid Earth*, 108(B6)

Figs. Captions

Fig. 1 Sketch map of the Aeolian archipelago and simplified geological map of Vulcano Island (modified after De Astis et al. 2013).

Fig. 2 (a) Stratigraphy of the deposits related to the last 1000 years of eruptive activity at La Fossa volcano (modified after Di Traglia et al. 2013); (b) Total alkali vs SiO₂ diagram showing whole rock data of La Fossa products erupted in the last 1000 years (cross symbols: pyroclastic products and lava flows, literature data; filled circles: products belonging to the eruptive units investigated in this work, literature data; stars: new whole rock data). Major elements are recalculated to 100% on anhydrous basis. Literature data from Clocchiatti et al. (1994), Del Moro et al. (1998), De Astis et al. (2013),

783 Nicotra et al. (2018), Pinarelli et al. (2019).

784

785

786

787

788

789

790

791

792

793

794

795

796

797

798

799

800

801

802

803

804

805

806

807

808

809

810

811

812

813

814

815

816

817

818

819

820

821

822

823

824

825

826

827

828

829

830

831

832

833

834

835

836

837

838

839

Fig. 3 Microphotographs of (a) a latitic crystal rich enclave of Pietre Cotte and host rhyolitic lava flow, (b) a latitic crystal rich enclave of Pietre Cotte, (c) the Palizzi trachytic lava and (d) the K-rich Pal D pumice; (e) Pal B rhyolitic pumice with magmatic enclave; (f) BSE image of a clinopyroxene in the rhyolitic pumice of Pal B, the crystal is wrapped by a microlitic corona isolating it from the rhyolitic groundmass glass (yellow line). Mineral abbreviations: Cpx, clinopyroxene; Pl, plagioclase; Sa, sanidine; Ti-Mt, Ti-magnetite.

Fig. 4 Feldspar ternary diagram showing the composition of feldspar phenocrysts in the investigated products. Data of plagioclase occurring in the latitic enclaves of Pietre Cotte are from Piochi et al. (2009) and this work.

Fig. 5 Diagrams showing Al^{IV}, Si, Ti, Mg cations (apfu, atom per formula unit) vs. the DiHd component of clinopyroxene in the investigated products. Data of clinopyroxene occurring in the latitic enclaves of Pietre Cotte are from Piochi et al. (2009) and this work.

Fig. 6 Chondrite-normalized Rare Earth Element (REE) patterns and Sr vs. Eu/Eu* for (a) plagioclase and (b) clinopyroxene. Data of plagioclase in the latitic enclaves of Pietre Cotte and Palizzi lava flow are from Piochi et al. (2009), Nicotra et al. (2018) and this work. Data of clinopyroxene in the latitic enclaves of Pietre Cotte are from Piochi et al. (2009).

Fig. 7 BSE images of experimental products at different temperature ranges and H₂O content. Phase abbreviations: Cpx, clinopyroxene; Afs, alkali-feldspar; Bt, biotite; Ox, oxide; Gl, glass.

Fig. 8 Crystallinity variation along the temperature gradient of the experiments. Phase abbreviations: Cpx, clinopyroxene; Afs, alkali-feldspar; Bt, biotite; Pl, plagioclase; Ox, oxide.

Fig. 9 Major elements variation diagrams of La Fossa products (symbols and references as reported in Fig. 2b) and experimental glasses. Major elements are recalculated to 100% on anhydrous basis.

Fig. 10 (a) Test of equilibrium for clinopyroxene comparing the observed and predicted values for DiHd component in clinopyroxene; (b) pressure and temperature estimates for the latitic and trachytic magmas at La Fossa obtained through clinopyroxene-liquid thermo-barometer of Masotta et al. (2013); (c,d) temperature inversion diagrams showing the linear least squares regression analyses of the REE partitioning data calculated for plagioclase-clinopyroxene pairs from Pal D K-rich pumice and Pietre Cotte latitic enclave using the REE-exchange thermometer of Sun and Liang (2017). D is the partition coefficient of a given element in the geochemical group of REE. A and B are coefficients corresponding to the changes of entropy and enthalpy. At the thermodynamic equilibrium, all elements in the same geochemical group define a straight line (best fit line passing through the origin) in a plot of ln(D)-A vs. B/1000, where temperature corresponds to the slope. Yellow dots are the data excluded from the regression analysis.

Fig. 11 Fractional crystallization modelling based on mass balance calculation using major element of bulk rocks and mineral of the eruptive products of La Fossa (symbols and references as reported in Fig. 2b). The starting composition is

824 represented by the latitic enclaves of Pietre Cotte, whereas the target compositions are the K-rich trachyte of Pal D
825 (segment 1), the trachyte of the Palizzi lava (segment 2) and the rhyolite of Pal B (segment 3 and 4). Only compositions
826 displaying a sum of squared residual (SSR) below 2 were considered.

827
828 **Fig. 12** (a) Assimilation and fractional crystallization (AFC) trace element modelling (symbols as reported in Fig. 2b).
829 r is the assimilation rate/fractionation rate. See supplementary material for the parameters used in the model and for ICP-
830 MS analyses of the Pal B rhyolite. Literature data from De Astis et al. (2013), Nicotra et al. (2018), Bullock et al. (2019),
831 Pinarelli et al. (2019).

832
833 **Fig. 13** (a) Sketch representation showing the depth of the reservoirs that have been active at La Fossa volcano in the
834 last 1000 years (depths and crustal structure after Peccerillo et al. 2006) and (b) of the extraction of crystal-poor rhyolite
835 from the crystal mush. The different interaction between the recharging magmas and the rhyolite explains the petrologic
836 features of the recent eruptive products of La Fossa.

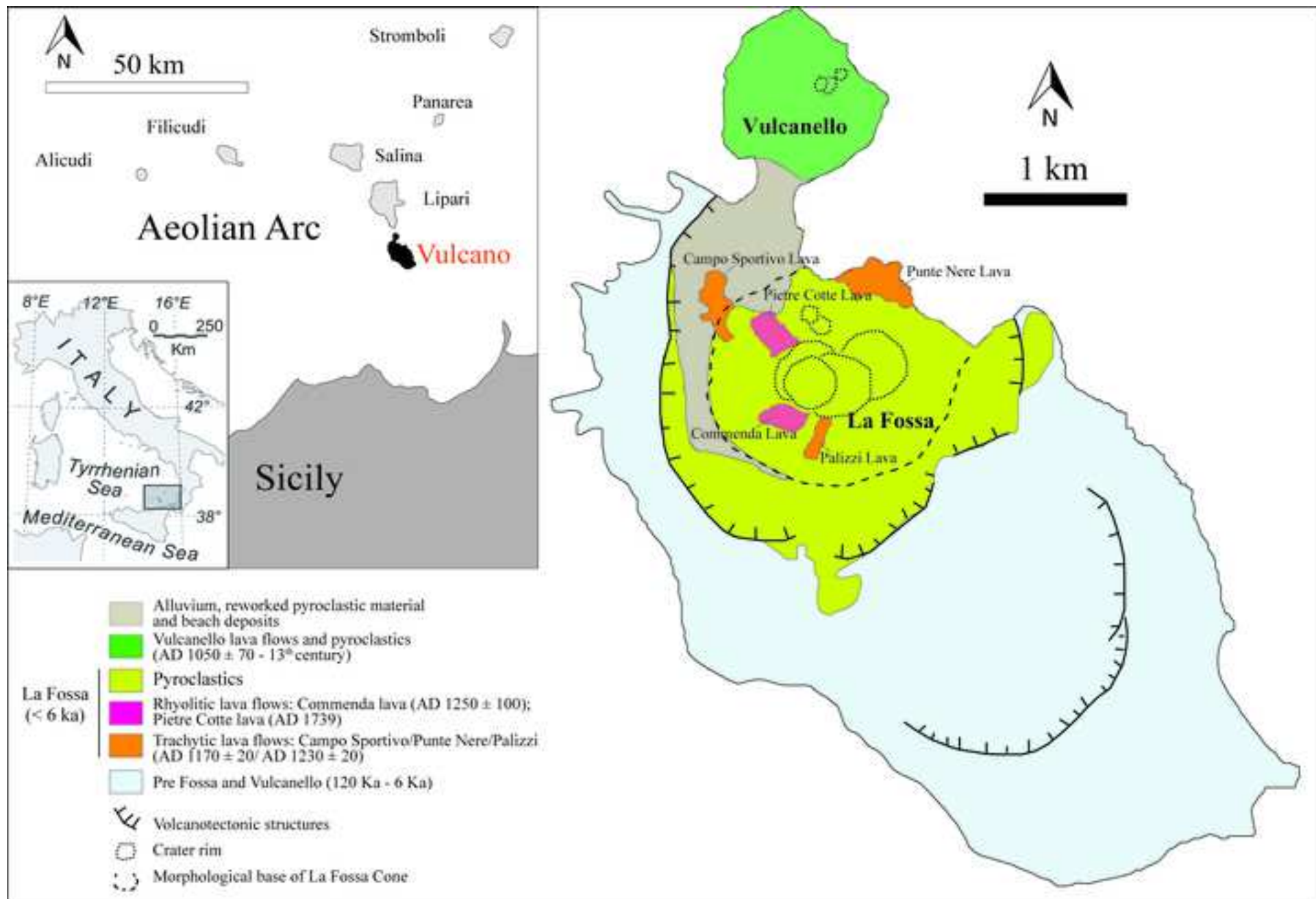
837
838 **Tables caption**

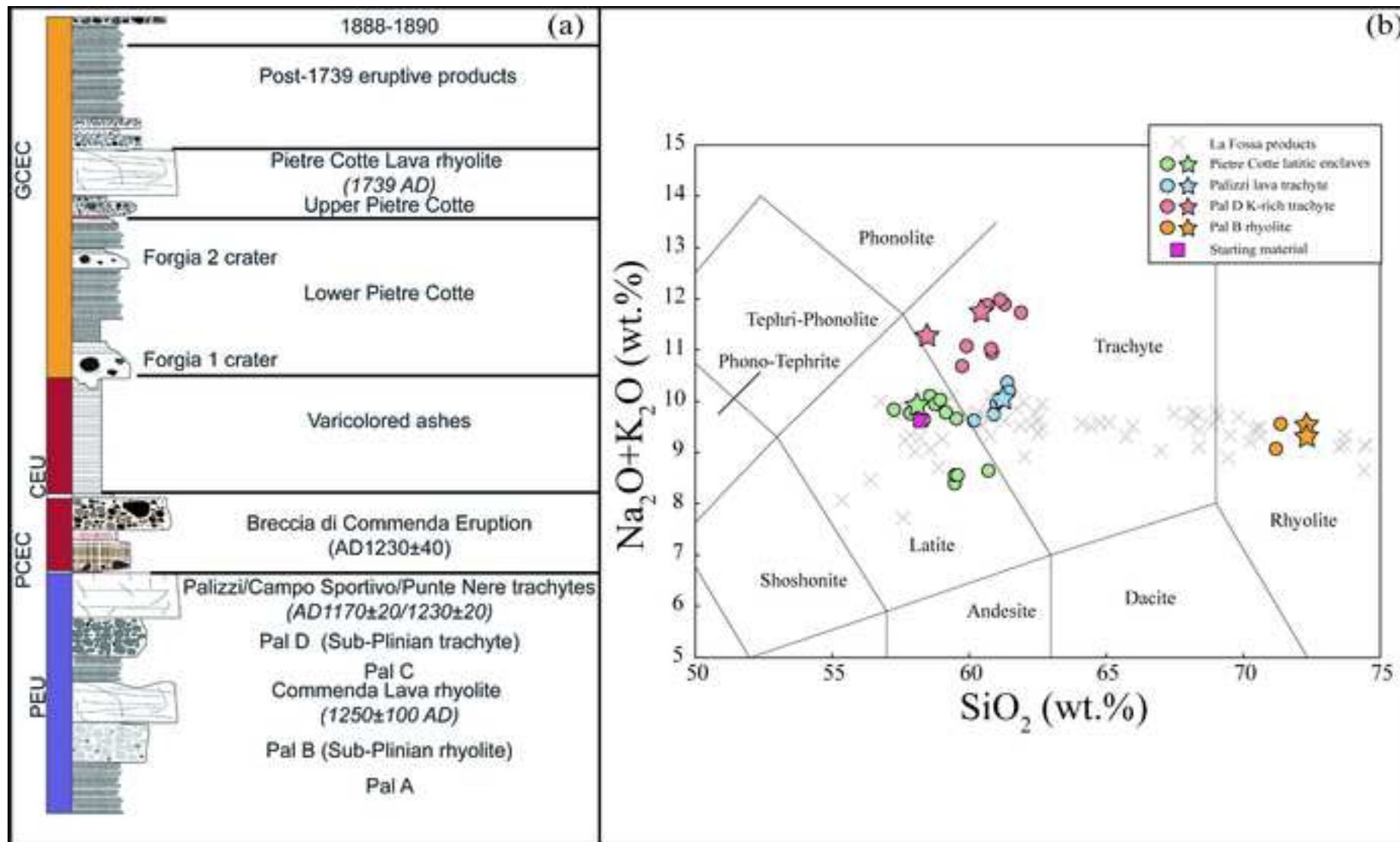
839
840 **Table 1** Whole rock XRF analyses of the eruptive products of La Fossa and EPMA analysis of the glass used as
841 starting material.

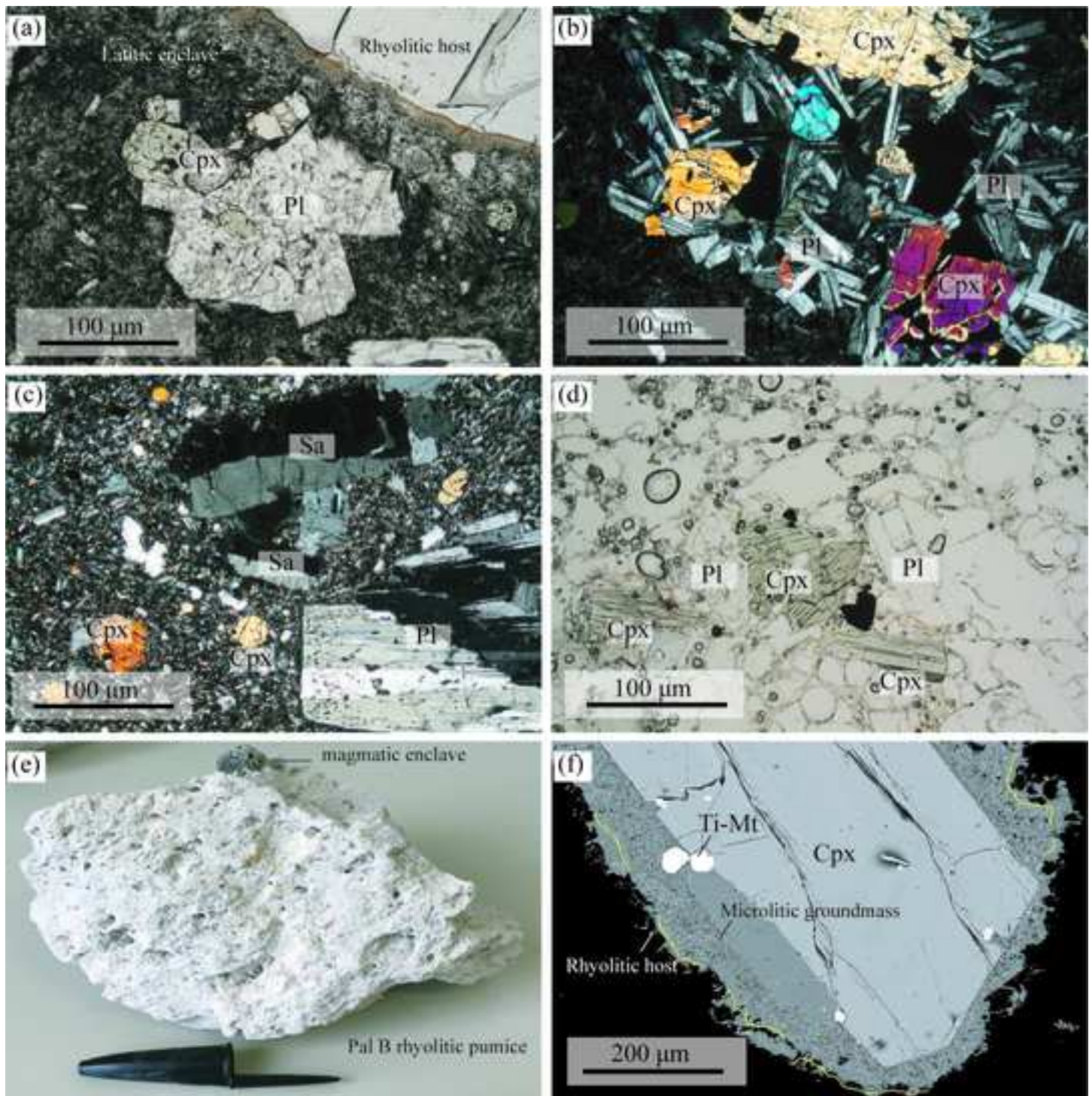
842
843 **Table 2** Phase proportions in experimental samples obtained through image analysis.

844
845 **Table 3** Temperature, pressure and H₂O estimates for the investigated products of La Fossa.

33
34
35
36
37
38
39
40
41
42
43
44
45
46
47
48
49
50
51
52
53
54
55
56
57
58
59
60
61
62
63
64
65







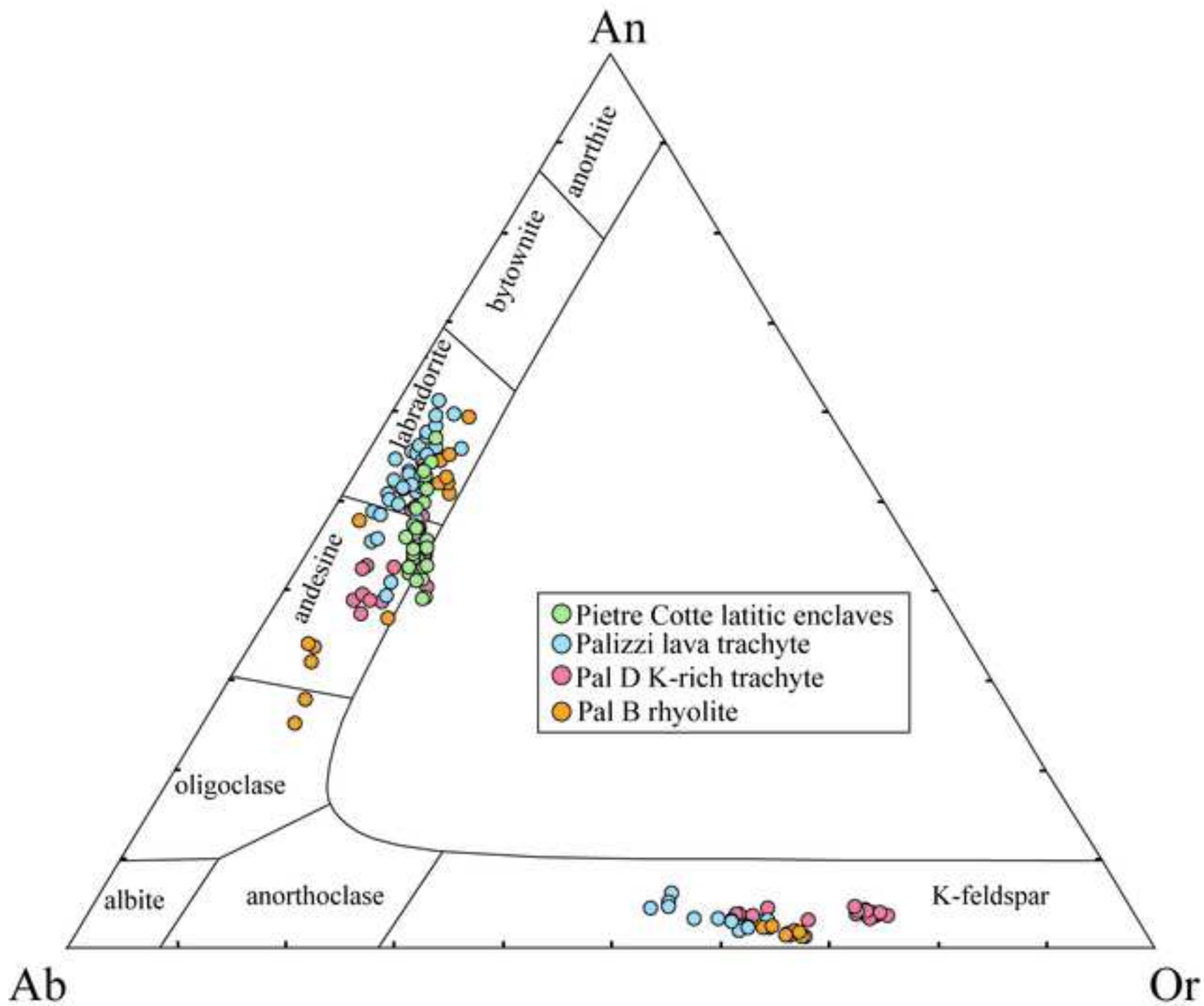
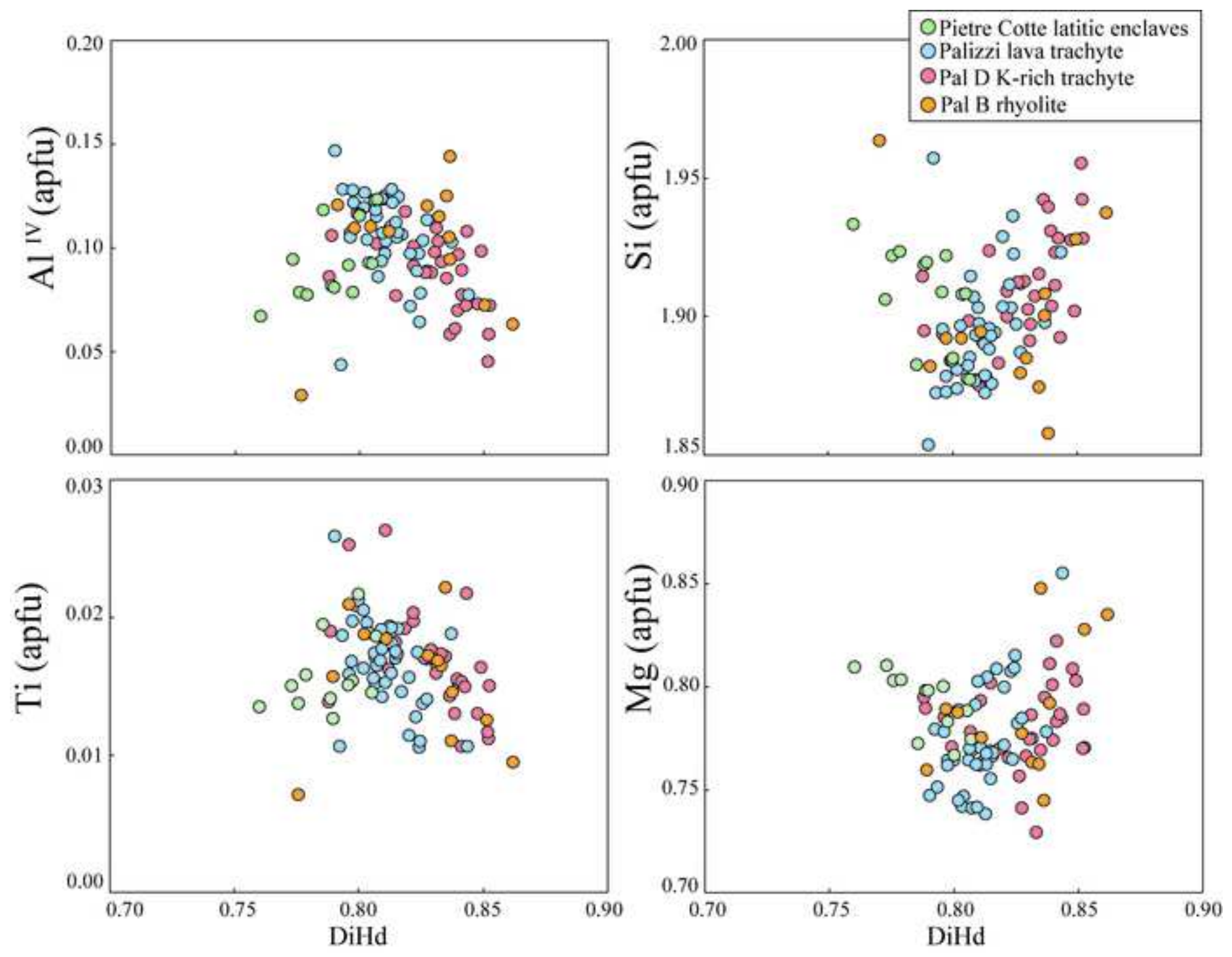
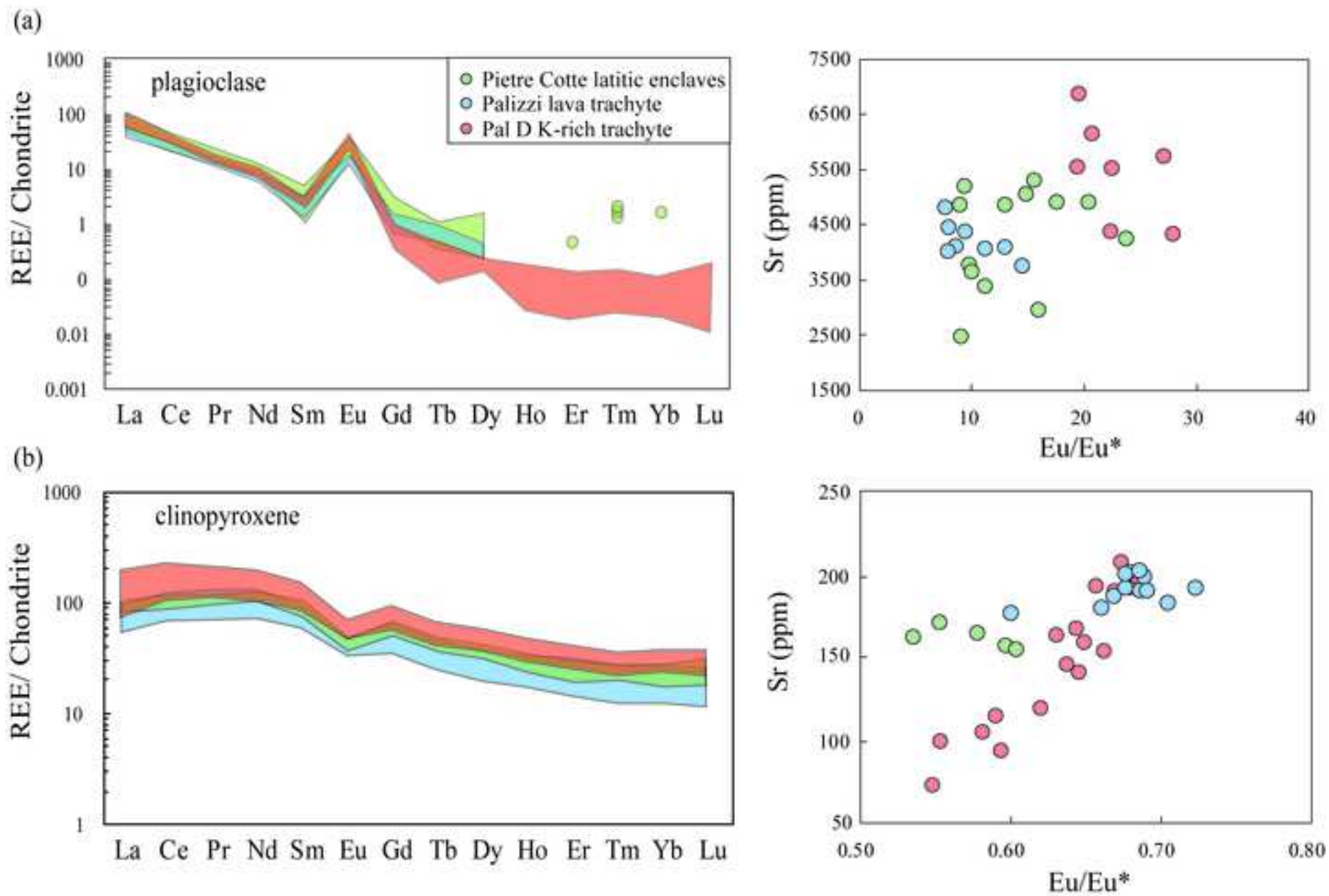


Figure 5

[Click here to access/download;Figure;figure5.tif](#)





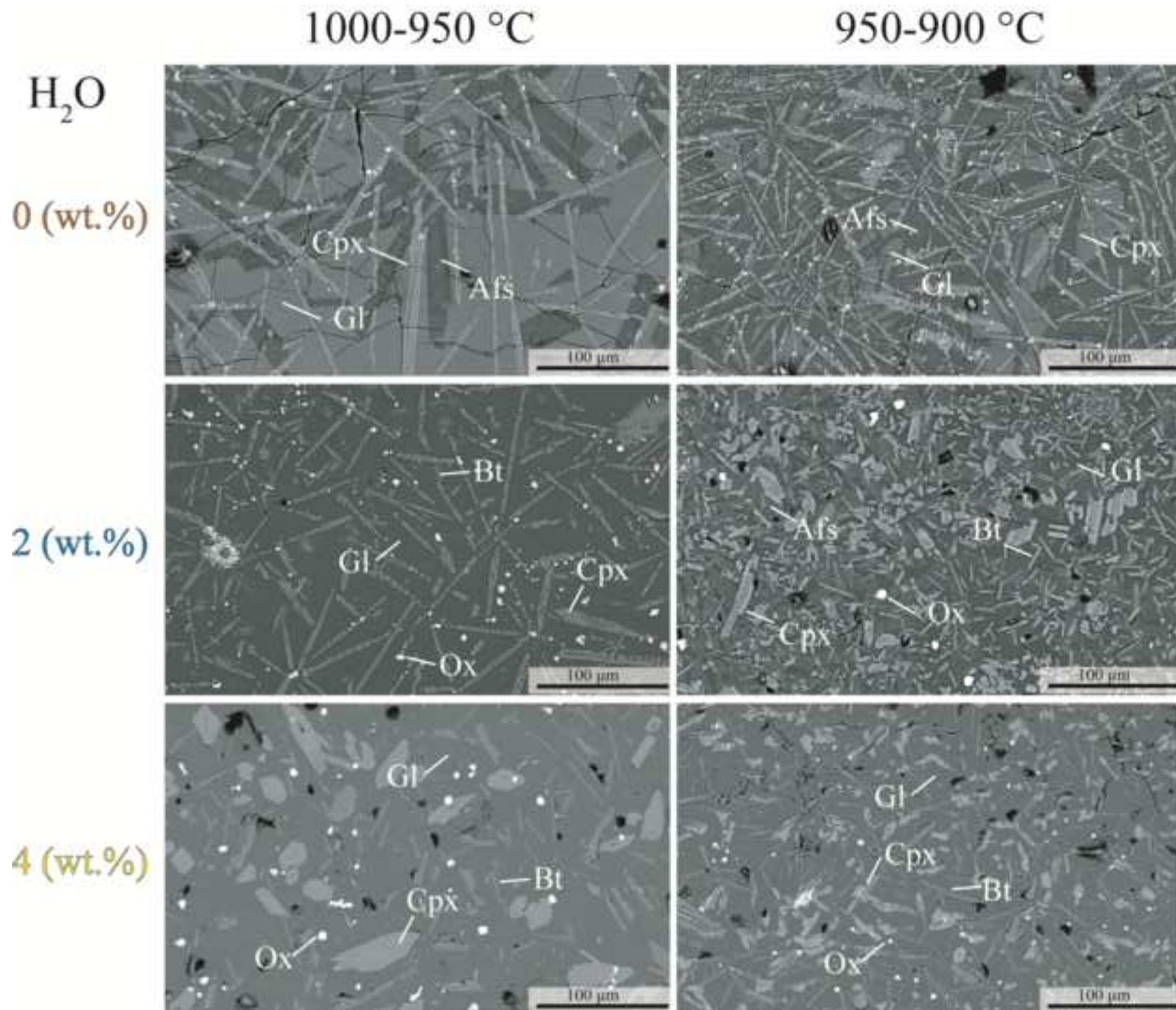
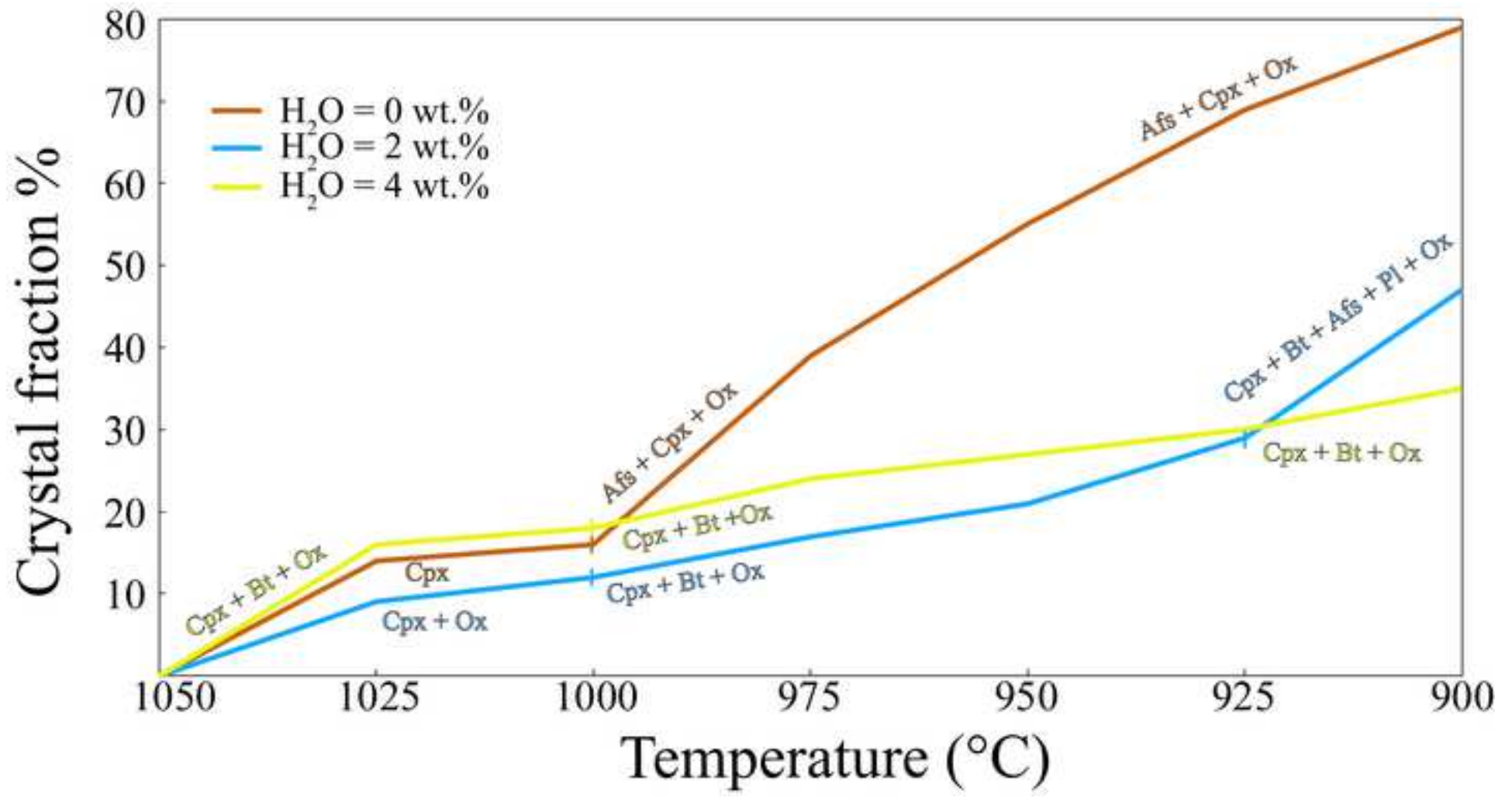
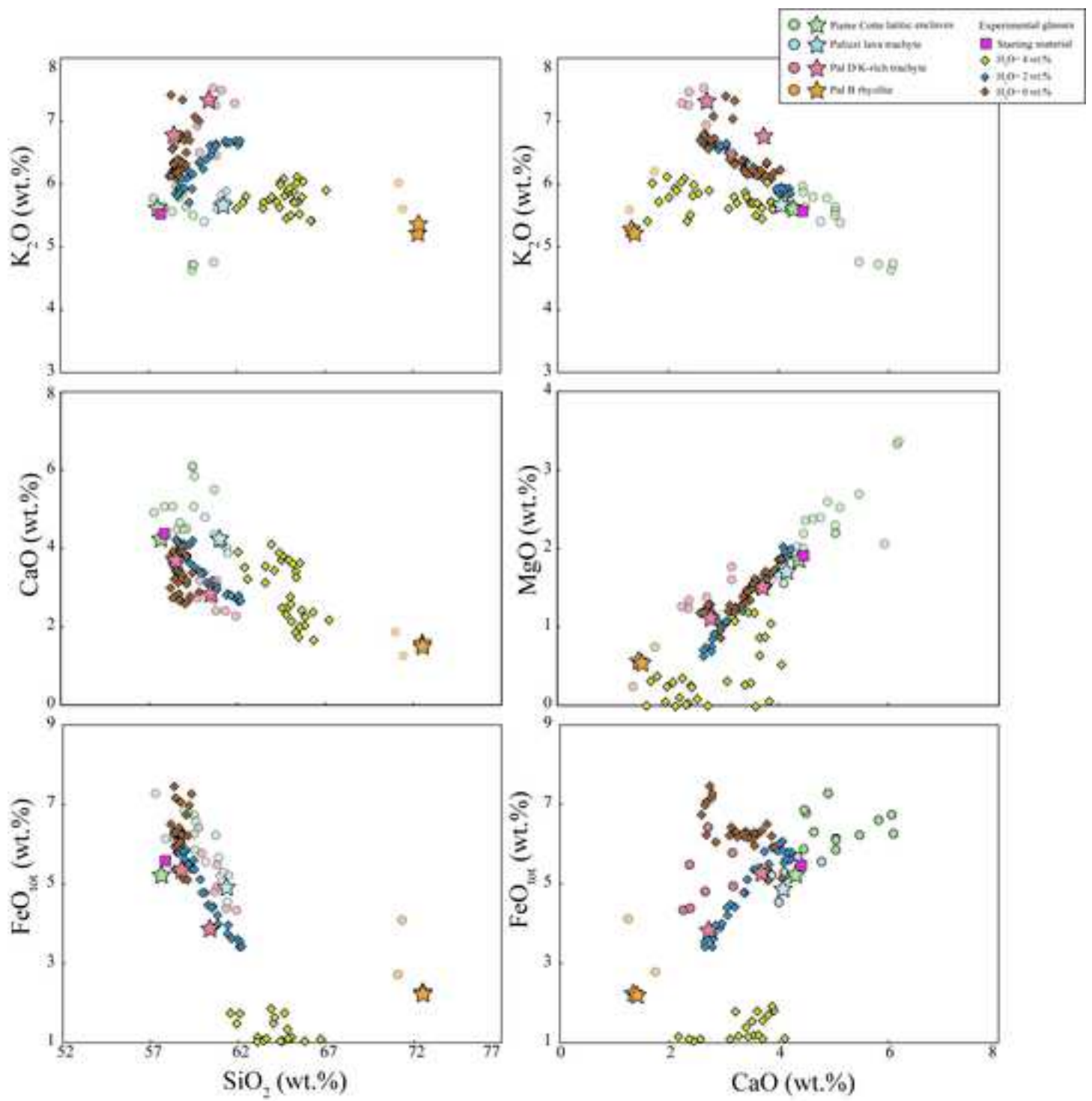
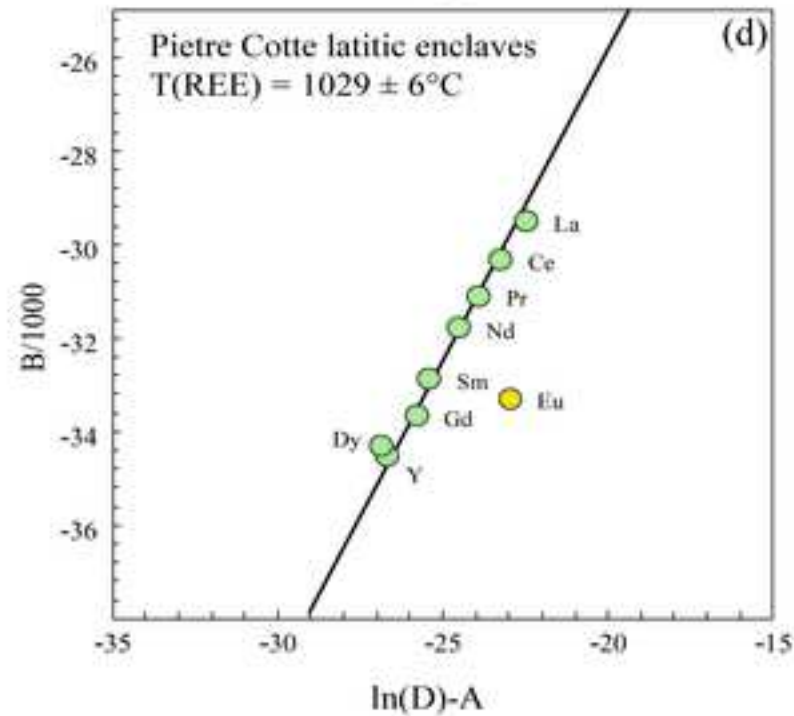
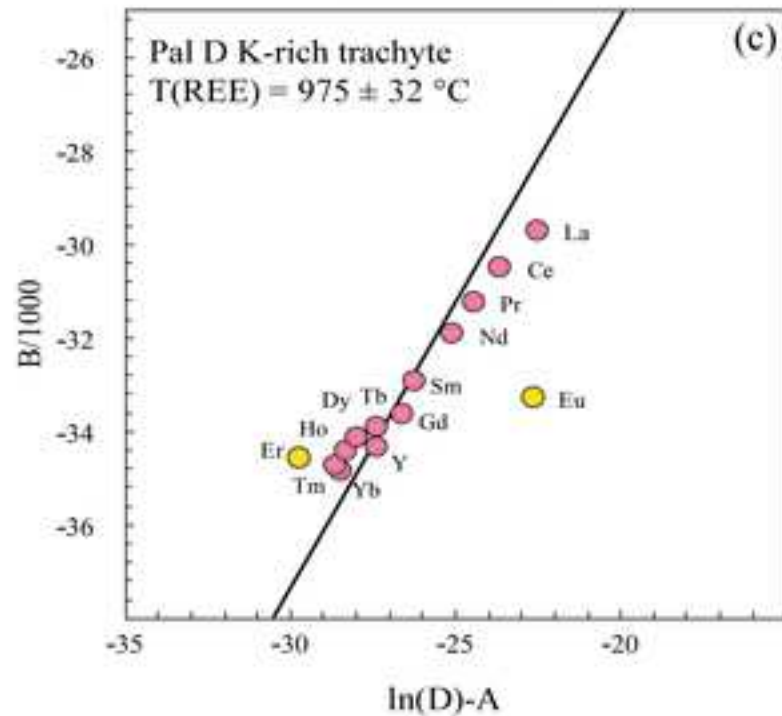
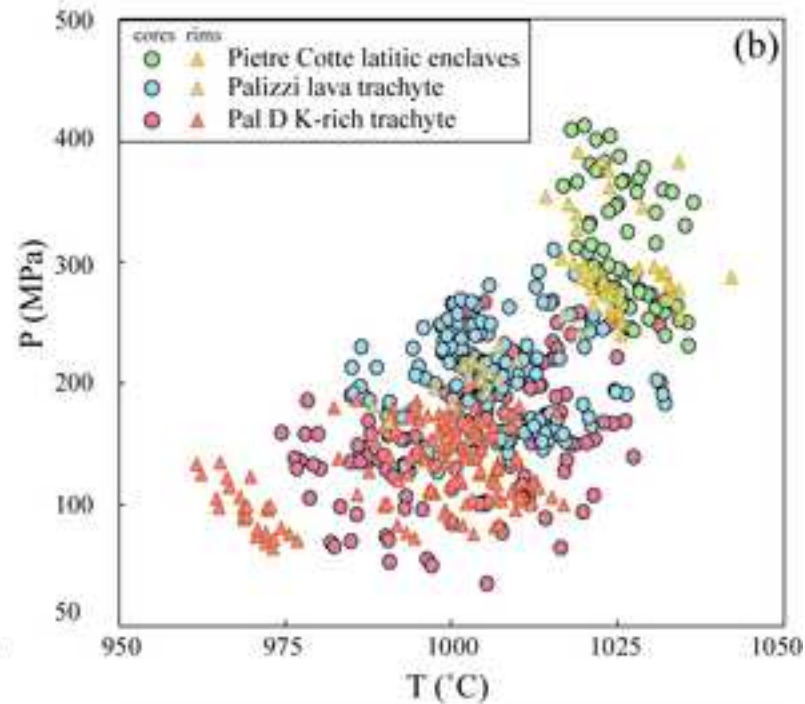
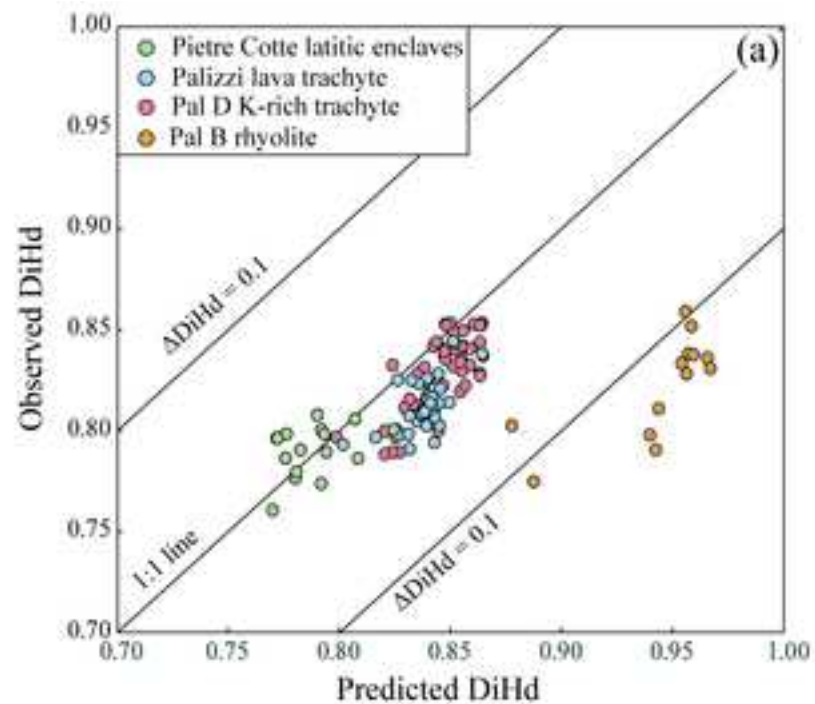
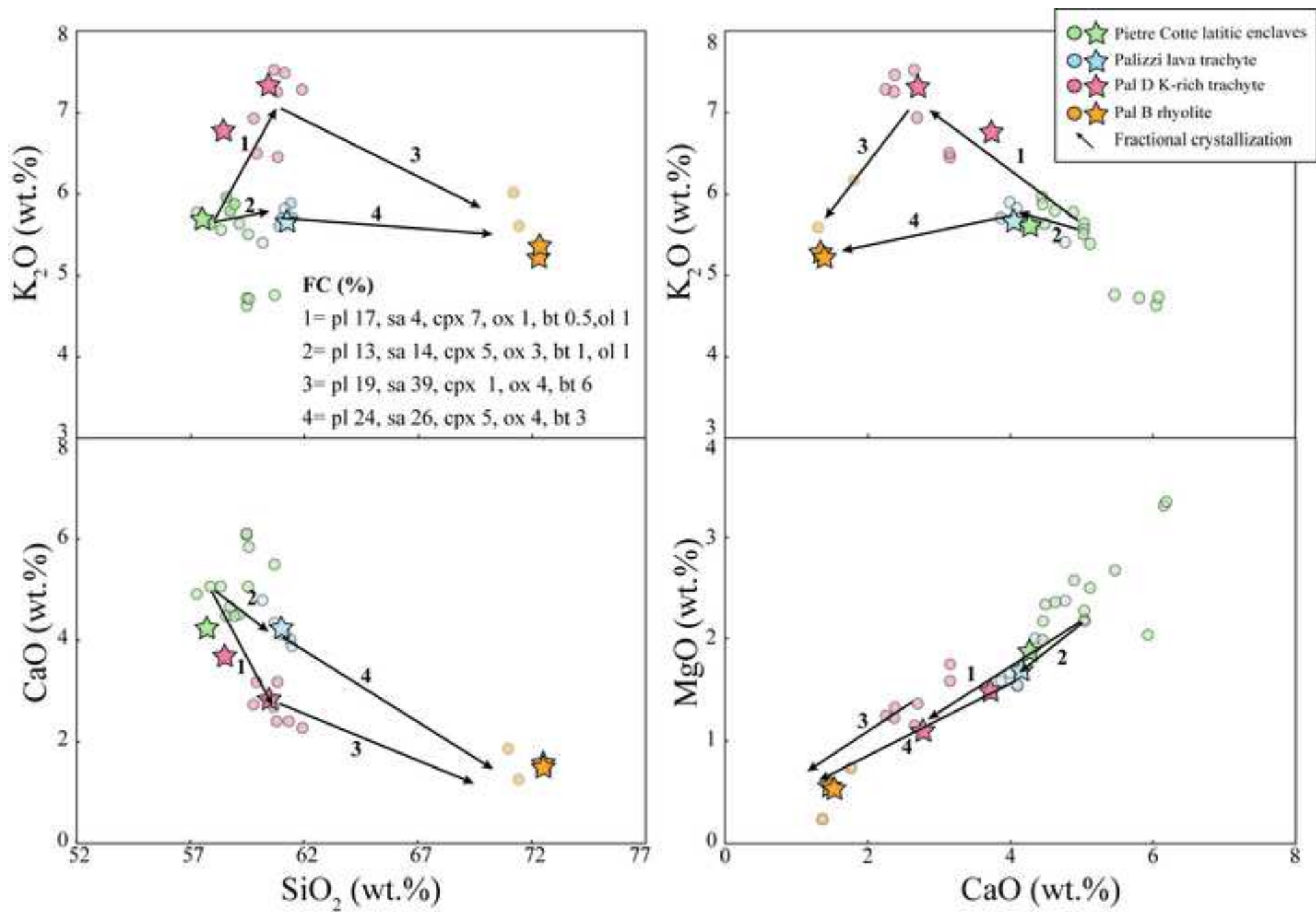


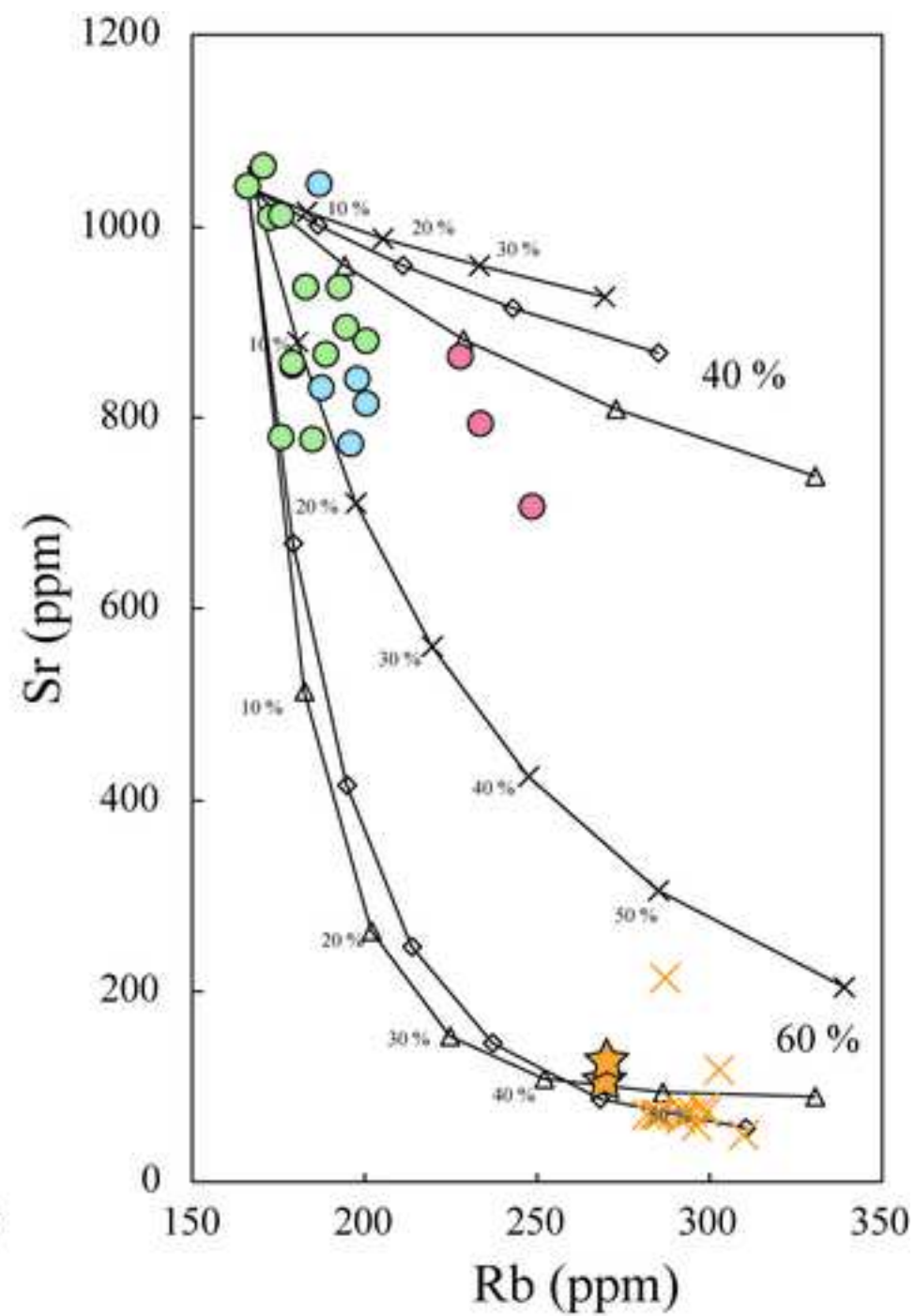
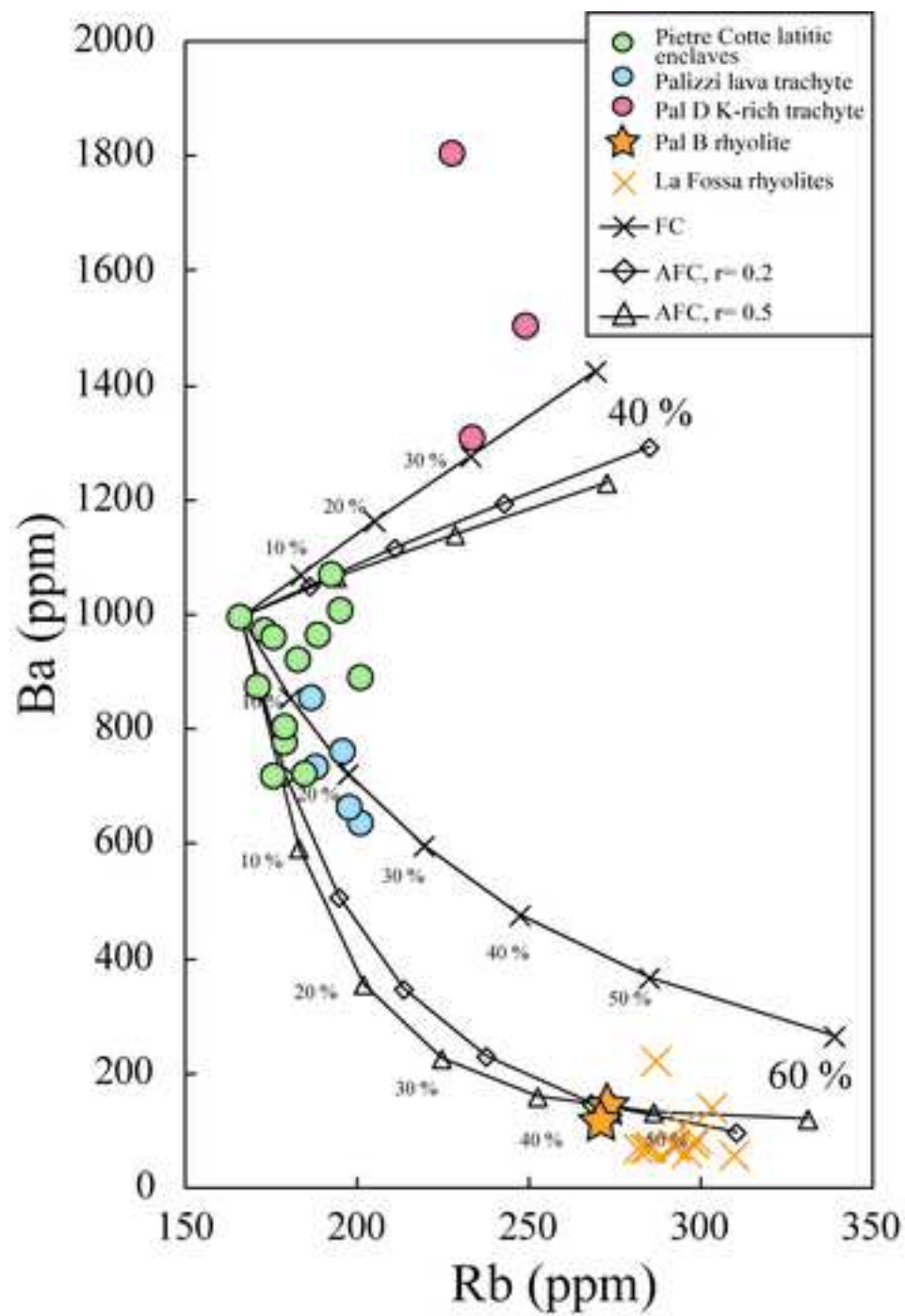
Figure 8











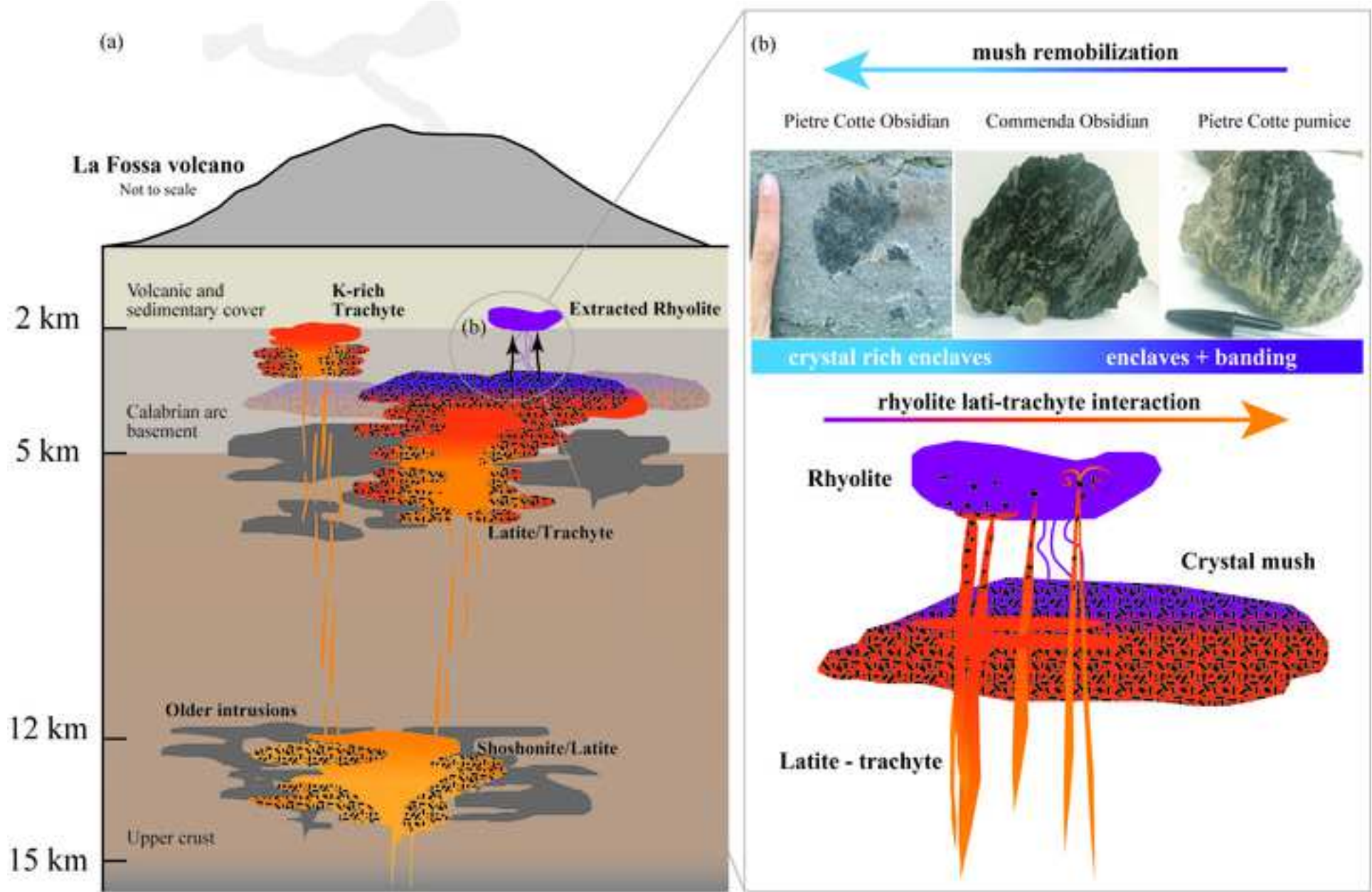


Table 1. Whole rock XRF analyses of the eruptive products of La Fossa and EPMA analysis of the glass used as starting material.

E.U.	Pal D	Pal D	Pal B	Pal B	Pietre Cotte	Palizzi	Starting Material	
Comp.	K-rich Trachyte	K-rich Trachyte	Rhyolite	Rhyolite	Latite	Trachyte	Latite	
Type	Pumice	Pumice	Pumice	Pumice	Enclave	Lava	glass	σ (10)
SiO₂	57.58	59.52	69.21	70.03	57.21	60.70	56.60	0.47
TiO₂	0.66	0.69	0.17	0.19	0.41	0.50	0.40	0.04
Al₂O₃	18.27	18.52	13.06	13.36	20.36	16.73	19.98	0.49
Fe₂O₃*	5.89	4.25	2.33	2.31	5.53	4.80	5.95*	0.22
MnO	0.11	0.10	0.07	0.07	0.13	0.15	0.12	0.02
MgO	1.50	1.13	0.51	0.51	1.83	1.77	1.90	0.07
CaO	3.63	2.68	1.40	1.44	4.18	4.20	4.48	0.21
Na₂O	4.41	4.37	3.98	3.94	4.23	4.39	3.92	0.12
K₂O	6.65	7.22	5.07	5.04	5.63	5.60	5.32	0.22
P₂O₅	0.43	0.32	0.09	0.10	0.31	0.30	0.28	0.05
Total	99.13	98.80	95.89	96.99	99.82	99.14	98.95	
L.O.I.	0.87	1.2	4.11	3.01	0.18	0.86	-	-

*Fe₂O_{3 tot} for XRF analyses of natural products, FeO_{tot} for EPMA analysis of the starting glass

Table 2. Phase proportions in experimental samples obtained through image analysis.

Phase (vol.%)	Temperature along the capsule (°C)					
	1050-1025	1025-1000	1000-975	975-950	950-925	925-900
<i>H₂O = 0 wt.%</i>						
Glass	86	84	61	45	30	20
Cpx	14	16	14	24	26	24
Afs	0	0	24	30	42	54
Ox	0	0	1	1	2	2
<i>H₂O = 2 wt.%</i>						
Glass	90	87	82	77	68	50
Cpx	8	11	14	17	19	24
Afs+Pl*	0	0	0	0	0	15
Ox	1	1	1	1	2	2
Bt	0	0	2	2	8	6
Vesicles	1	1	1	3	3	3
<i>H₂O = 4 wt.%</i>						
Glass	80	78	72	69	65	60
Cpx	6	7	13	13	13	15
Ox	1	1	1	2	2	2
Bt	9	10	10	12	15	18
Vesicles	4	4	4	4	5	5

*Alkali feldspar and plagioclase counted together because of the similar BSE intensity

Mineral abbreviations: Cpx: clinopyroxene; Afs: alkali feldspar; Pl: plagioclase; Ox: oxide; Bt: biotite

Table 3. Temperature, pressure and H₂O estimates for the investigated products of La Fossa.

Eruptive Unit		Pietre Cotte	Pal D	Palizzi	Pal B
Magma composition		Latite	K-rich Trachyte	Trachyte	Rhyolite
Product		Enclave	Pumice	Lava	Pumice
T (°C)	Cpx-liq (cores) ^a	1027±5	1004±14	1007±9	-
	Cpx-liq (rims) ^a	1025±6	996±13	1005±8	-
	REE in Cpx-Pl ^b	1037±8	991±31	1057±8	-
	Pl-liq ^c	-	-	-	952±7
P (MPa)	Cpx-liq (cores) ^a	307±47	160±54	199±39	-
	Cpx-liq (rims) ^a	294±38	132±33	208±30	-
H ₂ O (wt.%)	Pl-liq ^d	2.50-3.50 ^e	2.54±0.57	2.50-3.50 ^e	1.99±0.30

Model: ^aMasotta et al. (2013); ^bSun and Liang (2017); ^cPutirka (2008); ^dMasotta and Mollo (2019)

*Data from Masotta and Mollo (2019)